Big bang initial conditions and self-interacting hidden dark matter

Jinzheng Li* and Pran Nath†

Department of Physics, Northeastern University, Boston, Massachusetts 02115-5000, USA

(Received 6 September 2023; accepted 4 November 2023; published 11 December 2023)

A variety of supergravity and string models involve hidden sectors where the hidden sectors may couple feebly with the visible sectors via a variety of portals. While the coupling of the hidden sector to the visible sector is feeble, its coupling to the inflaton is largely unknown. It could couple feebly or with the same strength as the visible sector, which would result in either a cold or a hot hidden sector at the end of reheating. These two possibilities could lead to significantly different outcomes for observables. We investigate the thermal evolution of the two sectors in a cosmologically consistent hidden sector dark matter model where the hidden sector and the visible sector are thermally coupled. Within this framework, we analyze several phenomena to illustrate their dependence on the initial conditions. These include the allowed parameter space of models, dark matter relic density, proton-dark matter cross section, effective massless neutrino species at big bang nucleosynthesis time, self-interacting dark matter cross section, where self-interaction occurs via exchange of dark photon, and Sommerfeld enhancement. Finally, fits to the velocity dependence of dark matter cross sections from galaxy scales to the scale of galaxy clusters is given. The analysis indicates significant effects of the initial conditions on the observables listed above. The analysis is carried out within the framework where dark matter is constituted of dark fermions, and the mediation between the visible and the hidden sector occurs via the exchange of dark photons. The techniques discussed here may have applications for a wider class of hidden sector models using different mediations between the visible and the hidden sectors to explore the impact of big bang initial conditions on observable physics.

DOI: 10.1103/PhysRevD.108.115008

I. INTRODUCTION

Hidden sectors appear in most modern models of particle physics beyond the standard model and have become increasingly relevant in analyses of particle physics phenomena. Success of precision electroweak physics tell us that the hidden sector couplings to the standard model must be feeble, but what about the coupling of the hidden sector to the inflaton? If the coupling of the hidden sector to the inflaton is also feeble relative to the coupling of the standard model, the population of the hidden sector particles would be negligible, and their temperature would be much colder than of the standard model particles. On the other extreme, the hidden sector and the visible sectors could couple democratically, i.e., with equal strength, to the inflaton and thus be essentially in thermal equilibrium at the end of reheating. These cases represent two extreme

Published by the American Physical Society under the terms of the Creative Commons Attribution 4.0 International license. Further distribution of this work must maintain attribution to the author(s) and the published article's title, journal citation, and DOI. Funded by SCOAP³.

possibilities with a variety of other possibilities in between. Because of the interactions between the visible and the hidden sectors, the two sectors are thermally coupled, and thus, their evolution is constrained by the initial condition on the hidden sector at the end of inflation which can be codified by the ratio $\xi_0 \equiv T_h^0/T^0$, where T_h^0 is the temperature of the hidden sector, and T^0 is the temperature of the visible sector initially after reheating. It is thus of relevance to ask the influence of the initial conditions on physical observables at low energy. In this work, we study the effect of ξ_0 on a variety of physical observables, i.e., on the relic density of dark matter, on the proton-DM scattering cross sections, on the number of massless degrees of freedom at big bang nucleosynthesis (BBN), and on DM selfinteraction cross sections. For DM self-interaction cross section, we further analyze the effect of ξ_0 on its velocity dependence and on Sommerfeld enhancement and analyze the effect of ξ_0 on fits to the galactic dark matter cross sections from the scale of dwarf galaxies to the scale of galaxy clusters. The portal we utilize in the analysis consists of a hidden sector with a $U(1)_x$ gauge invariance with kinetic mixing [1] and Stueckelberg mass growth of the $U(1)_{\rm x}$ gauge boson [2]. By numerically solving the Schrödinger equation, we are able to achieve a comprehensive understanding of the dark matter self-interacting

li.jinzh@northeastern.edu p.nath@northeastern.edu

cross section in this model. While our analysis is done in a specific choice of the portal, one may expect similar effects discussed in this work using other portals connecting visible and the hidden sectors.

The outline of the rest of the note is as follows: Sec. II gives a summary of the thermal evolution of coupled visible and hidden sectors, while Sec. III discusses a specific model with the visible sector coupled to one hidden sector where the coupling arises via kinetic mixing along with Stueckelberg mass generation for the hidden sector gauge boson. Section IV discusses the effect of ξ_0 on dark freezeout and on the relic density of dark matter. Here, we also discuss the dependence of $\Delta N_{\rm eff}$ at BBN time on ξ_0 and further the effect of ξ_0 on the allowed parameter space and on the spin-independent proton-DM cross section. In Sec. V, we discuss the effect of ξ_0 on Sommerfeld enhancement for the self-interacting dark matter cross section. In Sec. VI, we discuss the effect of ξ_0 on fits to the galaxy data on dark matter cross sections from low relative velocities to high relative velocities, which encompass scales from dwarf galaxies to galaxy clusters. Conclusions are given in Sec. VII. Additional details related to the analysis are given in Appendix A-C. Further, in Appendix D, we give a comparison of our analysis of the thermal evolution when the total entropy is conserved vs the thermal evolution when the entropies of the visible and the hidden sectors are separately conserved. In this section, we also analyze the accuracy of using conservation of total entropy in computations of yields for dark matter since, in general, the total entropy is not conserved unless the sectors equilibrate.

II. COSMOLOGICALLY CONSISTENT EVOLUTION OF COUPLED VISIBLE AND HIDDEN SECTORS IN DM ANALYSIS

As mentioned in the previous section, most models of particle physics based on physics beyond the standard model contain hidden sectors that may be feebly coupled to the visible sector. In this case, the thermal evolution of each is interdependent on the other. Thus, the approximation typically made that the entropy of the visible and the hidden sectors are separately conserved is invalid. Further, the hidden sector by itself may consist of several sectors, some of which may interact directly with the visible sector while others indirectly via their interactions with other hidden sectors, which couple with the visible sector. First, in this case, the Hubble expansion is affected by the hidden sectors via their energy densities so that

$$H^{2} = \frac{8\pi G_{N}}{3} \left(\rho_{v} + \sum_{i=1}^{n} \rho_{i} \right), \tag{2.1}$$

where ρ_v is the energy density of the visible sector, and ρ_i the energy density of the *i*th hidden sector where $\rho's$ have temperature dependence so that

$$\rho = \frac{\pi^2}{30} \left(g_{\text{eff}}^v T^4 + \sum_{i=1}^n g_{i \, \text{eff}}^h T_i^4 \right), \tag{2.2}$$

and the total entropy density of the visible and hidden sectors is given by

$$s = \frac{2\pi^2}{45} \left(h_{\text{eff}}^v T^3 + \sum_{i=1}^n h_{i \text{ eff}}^h T_i^3 \right). \tag{2.3}$$

Here, $g_{\rm eff}^{v,h}$ and $h_{\rm eff}^{v,h}$ are the energy and entropy degrees of freedom and are temperature dependent. A full expression for them for the specific model we will consider is given in Sec. III. In [3], an analysis was given where the visible sector (V) at temperature T is coupled to the hidden sector H_1 at temperature T_1 , the hidden sector H_1 is coupled to the hidden sector H_2 at temperature T_2 , and so on, and finally that the hidden sector H_n at temperature T_n . In the analysis of [3], radiation dominance was assumed. Here, we extend the analysis to include radiation and matter. In this case, the energy densities for various sectors obey the following set of coupled Boltzmann equations:

$$\frac{d\rho_{\alpha}}{dt} + 3H(\rho_{\alpha} + p_{\alpha}) = j_{\alpha}, \qquad \alpha = 0, 1, 2, ..., n.$$
 (2.4)

Here, ρ_{α} and p_{α} are the energy and momentum densities for the sector α , where $\alpha=0$ refers to the visible sector, and $\alpha=1,2,...,n$ to the hidden sectors, and where j_{α} encodes in it all the possible processes exchanging energy between neighboring sectors. We note now that the total energy density $\rho=\sum_{\alpha=0}^{n}\rho_{\alpha}$ in an expanding universe satisfies the equation

$$\frac{d\rho}{dt} + 3H(\rho + p) = 0, (2.5)$$

where $p=\sum_{\alpha=0}^n \rho_\alpha$ is the total pressure density. In the analysis, it is convenient to introduce the functions $\zeta=\frac{3}{4}(1+\frac{p}{\rho})$ and $\zeta_\alpha=\frac{3}{4}(1+\frac{p_\alpha}{\rho_\alpha})$, where $\zeta_\alpha=1$ for radiation dominance and $\zeta_\alpha=\frac{3}{4}$ for matter dominance. More generally, ζ and ζ_α are temperature dependent, and this dependence is taken into account in the evolution equations. Thus, ρ_α and ρ satisfy the evolution equations:

$$\frac{d\rho_{\alpha}}{dt} + 4H\zeta_{\alpha}\rho_{\alpha} = j_{\alpha}, \qquad (2.6)$$

$$\frac{d\rho}{dt} + 4H\zeta\rho = 0. (2.7)$$

We use the visible sector temperature T as the clock as we thus wish to write the evolution equations Eqs. (2.6)

and (2.7) in terms of temperature T rather than time. This is accomplished using the relation

$$\frac{dT}{dt} = -\frac{4H\zeta\rho}{\frac{d\rho}{dT}}. (2.8)$$

Thus, using $d\rho_{\alpha}/dt = (d\rho_{\alpha}/dT)(dT/dt)$, one has

$$\frac{d\rho_{\alpha}}{dT} = \frac{(4H\zeta_{\alpha}\rho_{\alpha} - j_{\alpha})}{4H\zeta\rho} \frac{d\rho}{dT}.$$
 (2.9)

Next decomposing ρ so that $\rho = \rho_v + \sum_{i=1}^n \rho_i$, one finds that $d\rho_i/dT$ can be written as

$$\frac{d\rho_i}{dT} = \sum_{i=1}^n (\mathcal{C}^{-1})_{ij} C_j \frac{d\rho_v}{dT}.$$
 (2.10)

Here,

$$C_i = \frac{4H\zeta_i \rho_i - j_i}{4H\sigma_i + j_i},\tag{2.11}$$

where $\sigma_i = \zeta \rho - \zeta_i \rho_i$, and C_{ij} is defined so that

$$C_{ij} = \delta_{ij} - C_i (i \neq j), i, \quad j = 1, 2, ..., n.$$
 (2.12)

Note that one may also write

$$\frac{d\rho_i}{dT} = P_i + Q_i \xi_i', \quad i = 1, 2, ..., n.$$
 (2.13)

Here, $P_i = \xi_i \frac{d\rho_i}{dT_i}$, $Q_i = T \frac{d\rho_i}{dT_i}$, where $\xi_i = T_i/T$ and $\xi_i' \equiv d\xi_i/dT$. Thus, we have an equation for $d\xi_i/dT$, which takes the form

$$\frac{d\xi_i}{dT} = -\frac{P_i}{Q_i} + \sum_{i=1}^n (\mathcal{C}^{-1})_{ij} C_j \frac{\rho_v'}{Q_i}; \quad i = 1, 2, ..., n, \quad (2.14)$$

where $\rho'_v = d\rho_v/dT$. Equations (2.14) give us a set of n differential equations for the evolution functions $d\xi_i/dT$. These have to be solved along with the Boltzmann equations governing the number density evolution of the hidden sector particles. This will allow us to determine the relic densities of all stable species and describe the thermal evolution of this coupled system. For the case of the visible sector coupled to one hidden sector, we have $C_{11} = 1$, $C_1 = (4H\zeta_h\rho_h - j_h)/(4H\zeta\rho - 4H\zeta_h\rho_h + j_h)$, $\rho_h \equiv \rho_1$, $T_h \equiv T_1$, $j_h \equiv j_1$, and we define $\xi \equiv \xi_1 = T_h/T$. The source term j_h is discussed in Appendix A. With this notation specific to the case of the visible sector and one hidden sector, we have the following equation for ξ , which governs the temperature evolution of the hidden sector relative to that of the visible sector

$$\frac{d\xi}{dT} = \left[-\xi \frac{d\rho_h}{dT_h} + \frac{4H\zeta_h\rho_h - j_h}{4H\zeta\rho - 4H\zeta_h\rho_h + j_h} \frac{d\rho_v}{dT} \right] \left(T \frac{d\rho_h}{dT_h} \right)^{-1}.$$
(2.15)

We note that $g_{\rm eff}^v$ and $h_{\rm eff}^v$ are precalculated, and we use tabulated results from micrOMEGAs [4]. As noted already, $g_{\rm eff}^h$ and $h_{\rm eff}^h$ for the hidden sector that enter Eqs. (2.2) and (2.3) are temperature dependent [5,6], and their explicit expressions are given in Eq. (B4).

III. THE MODEL COUPLING VISIBLE AND HIDDEN SECTORS

There are a variety of portals that allow communication between the visible and the hidden sectors. These include the Higgs field portal [7], kinetic mixing of two gauge fields [1], Stueckelberg mass mixing [2,8], kinetic and Stueckelberg mass mixing [9], Higgs-Stueckelberg portal [10], as well as other possibilities such as higher dimensional operators. In this work, we focus on kinetic mixing along with the mass growth for the hidden sector gauge field via the Stueckelberg mechanism. Thus, for analysis in this work, we consider a specific model for dark matter, which is an extension of the standard model with an $SU(3) \times SU(2) \times U(1)_Y \times U(1)_X$ gauge invariance where the $U(1)_X$ gauge field has kinetic mixing with the visible sector $U(1)_V$ gauge field [1] and, in general, a Stueckelberg mass mixings [2,9,11,12]. We assume that the $U(1)_{x}$ hidden sector has a dark fermion D, which interacts with the $U(1)_{\rm x}$ gauge field. Thus, the extended $SU(3) \times$ $SU(2) \times U(1)_Y \times U(1)_X$ Lagrangian consisting of the SM part \mathcal{L}_{SM} and the extended part \mathcal{L}_{ext} is given by

$$\mathcal{L} = \mathcal{L}_{\text{SM}} + \mathcal{L}_{\text{ext}},$$

$$\mathcal{L}_{\text{ext}} = -\frac{1}{4} C^{\mu\nu} C_{\mu\nu} - \bar{D} \left(\gamma^{\mu} \frac{1}{i} \partial_{\mu} + m_D \right) D - g_X \bar{D} Q_X \gamma^{\mu} D C_{\mu}$$

$$-\frac{\delta}{2} C^{\mu\nu} B_{\mu\nu} - \frac{1}{2} (M_1 C_{\mu} + M_2 B_{\mu} + \partial_{\mu} \sigma)^2. \tag{3.1}$$

Here B_{μ} is the gauge field for the $U(1)_Y$, C_{μ} is the gauge field of $U(1)_X$, σ is an axionic field that gives mass to C_{μ} and is absorbed in the unitary gauge, and D is the dark fermion where Q_X is the $U(1)_X$ charge of D and g_X is gauge coupling of $U(1)_X$. Further, δ is the kinetic mixing parameter between the field strengths of C^{μ} and B^{μ} , and M_1 and M_2 are the Stueckelberg mass parameters. A nonvanishing M_2 will lead to a milli-charge for the dark fermion D, and we assume neutrality of dark matter and thus set $M_2 = 0$ in the analysis. The spontaneous breaking of the $SU(2) \times U(1)_Y$ electroweak symmetry along with the Stueckelberg mass growth gives rise to mixing among

 $^{^{1}}$ A nonvanishing M_{2} was used to resolve the EDGES anomaly in the analysis of [13].

the three gauge fields C^{μ} , B^{μ} , A^{μ}_3 , where A^{μ}_a is the third component of the $SU(2)_L$ gauge field A^{μ}_a (a=1,2,3) of the standard model. The mixings give rise to a 3×3 mass square matrix, which can be diagonalized by the three Euler angles (θ,ϕ,ψ) , which are given in Eq. (B3). The diagonalization gives the following mass eigenstates: the Z boson, a massive dark photon γ' , and the massless photon γ . The Lagrangian governing the interaction of dark photon and dark fermion, which enters into our analysis, is given by

$$\mathcal{L}_{\text{dark}} = -\frac{1}{4} A_{\mu\nu\gamma'} A^{\mu\nu}_{\gamma'} - \frac{1}{2} m^2_{\gamma'} A_{\gamma'\mu} A^{\mu}_{\gamma'} - \bar{D} \left(\gamma^{\mu} \frac{1}{i} \partial_{\mu} + m_D \right) D$$
$$- \bar{D} \gamma^{\mu} [\epsilon^D_Z Z_{\mu} + g^D_{\gamma'} A^{\gamma'}_{\mu}] D. \tag{3.2}$$

The interaction of Eq. (3.2) involves two massive gauge bosons (Z, γ') . For the case when the kinetic mixing is small, one has $g_{\gamma'}^D \simeq g_X Q_X$ and $\epsilon_Z^D = O(\delta^3)$, which is negligible. In addition, the dark photon will have couplings with the standard model quarks and leptons, which are discussed in Appendix C. Setting $Q_X = 1$, the input parameters of the model are $g_X, m_D, m_{\gamma'}, \delta$, which are what appear in Table I. We note here that models with the vector boson as the mediator between the hidden sector and the visible sector have been considered in several previous works [14–56]. Axions and dark photons in the light to ultralight mass region have also been investigated [45,47,57–61], and dark photons have been used in explaining astro-physical phenomena including galactic γ rays [62,63] and PAMELA positron excess [64–68].

We further note that the dark photon in this model even when very light and kinematically disallowed to decay into e^+e^- will eventually decay via the modes $\gamma' \to \nu\bar{\nu}$ and $\gamma' \to 3\gamma$ and not contribute to dark matter density unless its lifetime is larger than the lifetime of the Universe and, even in that case, only if it has non-negligible relic density, which is not the case we consider. Thus, the dark fermion will be the only constituent of dark matter. Further details about this model are given in Appendix B.

IV. BIG BANG CONSTRAINTS ON DARK FREEZE-OUT, RELIC DENSITY, $\Delta N_{\rm eff}$, AND ON PROTON-DM CROSS SECTION

In this section, we discuss the effects on the relic density, on the number of relativistic degrees of freedom due to the hidden sector at the BBN time, on the allowed parameter space of models, and on the proton-dark matter scattering cross section arising from different choices of the initial value ξ_0 at the end of reheating. In the model discussed in the preceding section, the dark fermion D constitutes dark matter and has self-interactions due to exchange of dark photon.

A. Effect of ξ_0 on dark freeze-out and on relic density

In the analysis here, we will discuss the effect of ξ_0 on the dark freeze-out, which generates the relic density of D. Computationally, the quantities of interest for this purpose are the yields for the dark fermion Y_D and for the dark photon $Y_{\gamma'}$, where the yield is defined so that Y = n/s, where n is the number density, and s is the entropy density. Assuming conservation of total entropy (this assumption will be tested in Appendix D), the evolution equations for Y_D and $Y_{\gamma'}$ are given by

$$\frac{dY_D}{dT} = -\frac{\mathrm{S}}{H} \left(\frac{d\rho_v/dT}{4\zeta\rho - 4\zeta_h\rho_h + j_h/H} \right) [\langle \sigma v \rangle_{D\bar{D} \to i\bar{i}}(T) Y_D^{\mathrm{eq}}(T)^2 - \langle \sigma v \rangle_{D\bar{D} \to \gamma'\bar{\gamma'}}(T_h) Y_D(T_h)^2 + \langle \sigma v \rangle_{\gamma'\bar{\gamma'} \to D\bar{D}}(T_h) Y_{\gamma'}(T_h)^2], \tag{4.1}$$

$$\frac{dY'_{\gamma}}{dT} = -\frac{s}{H} \left(\frac{d\rho_{v}/dT}{4\zeta\rho - 4\zeta_{h}\rho_{h} + j_{h}/H} \right) [\langle \sigma v \rangle_{D\bar{D} \to \gamma'\bar{\gamma'}} (T_{h}) Y_{D} (T_{h})^{2} - \langle \sigma v \rangle_{\gamma'\bar{\gamma'} \to D\bar{D}} (T_{h}) Y_{\gamma'} (T_{h})^{2} + \langle \sigma v \rangle_{i\bar{i} \to \gamma'} (T) Y_{i}^{\text{eq}} (T)^{2} - \langle \Gamma_{\gamma' \to i\bar{i}(T_{h})} \rangle Y_{\gamma'} (T_{h})].$$
(4.2)

Here, $\langle \sigma v \rangle_{D\bar{D} \to i\bar{i}}$ is the annihilation cross section of $D\bar{D}$ into standard model particles, which are denoted by $i\bar{i}$, $\langle \sigma v \rangle_{D\bar{D} \to \gamma'\gamma'}$ is their annihilation into dark photon, while $\langle \sigma v \rangle_{i\bar{i} \to \gamma'}$ gives the annihilation of standard model particles into a dark photon, and n_D and $n_{\gamma'}$ are the number densities of the D fermion and the dark photon γ' . In the above, the cross section for the process $D\bar{D} \to \gamma'\gamma'$ is given by

$$\sigma^{D\bar{D}\to\gamma'\gamma'}(s) = \frac{g_X^4(\mathcal{R}_{11} - s_{\delta}\mathcal{R}_{21})^4}{8\pi s(s - 4m_D^2)} \left\{ -\frac{\sqrt{(s - 4m_{\gamma'}^2)(s - 4m_D^2)}}{m_{\gamma'}^4 + m_D^2(s - 4m_{\gamma'}^2)} [2m_{\gamma'}^4 + m_D^2(s + 4m_D^2)] + \log\left[\frac{s - 2m_{\gamma'}^2 + \sqrt{(s - 4m_{\gamma'}^2)(s - 4m_D^2)}}{s - 2m_{\gamma'}^2 - \sqrt{(s - 4m_{\gamma'}^2)(s - 4m_D^2)}} \right] \frac{(s^2 + 4m_D^2s + 4m_{\gamma'}^4 - 8m_D^4 - 8m_D^2m_{\gamma'}^2)}{s - 2m_{\gamma'}^2} \right\},$$
(4.3)

while the rest of the cross sections are given in Appendix of [13]. Here s, t, u are Mandelstam variables, where $s+t+u=2m_D^2+2m_{\gamma'}^2$, \mathcal{R}_{11} and \mathcal{R}_{21} are matrix elements of \mathcal{R} , which diagonalizes the mass and kinetic energy matrices of Eq. (3.1) as given in [9]. Further, we note that in addition to $D\bar{D} \to \gamma'\gamma'$, we also have $\gamma'\gamma' \to D\bar{D}$, which enters in the yield equations when kinematically allowed and is related to $D\bar{D} \to \gamma'\gamma'$ so that

$$9(s - 4m_{\nu'}^2)\sigma^{\gamma'\gamma' \to D\bar{D}}(s) = 8(s - 4m_D^2)\sigma^{D\bar{D} \to \gamma'\gamma'}(s).$$
 (4.4)

In the above equation, the thermally averaged cross section and decay widths are given by

$$\begin{split} \langle \sigma v \rangle^{a\bar{a} \to bc}(T) &= \frac{1}{8m_a^4 T K_2^2(m_a/T)} \int_{4m_a^2}^{\infty} ds \sigma(s) \sqrt{s} (s - 4m_a^2) \\ &\times K_1(\sqrt{s}/T), \end{split} \tag{4.5}$$

$$\langle \Gamma_{X \to i\bar{i}}(T) \rangle = \Gamma_{x \to i\bar{i}} \frac{K_1(m_X/T)}{K_2(m_X/T)}.$$
 (4.6)

The equilibrium yield of the i-th particle is given by

$$Y_i^{\text{eq}} = \frac{n_i^{\text{eq}}}{s} = \frac{g_i}{2\pi s} m_i^2 T K_2(m_i/T),$$
 (4.7)

where s is the entropy density. In Eqs. (4.5)–(4.7), K_1 and K_2 are the modified Bessel functions of the second kind and of degrees one and of degree two. Further, cross sections for the processes $D\bar{D} \to i\bar{i}$, where i,\bar{i} are the standard model particles, can be found in Appendix D of [69]. As noted above, in this model, the dark photon is unstable and decays and does not contribute to the relic density, and the entire DM relic density arises from the dark fermion, where at current times, the relic density $\Omega_D h^2$ is given by

$$\Omega_D h^2 = \frac{\mathsf{s}_0 m_D Y_D^0 h^2}{\rho_c} \,, \tag{4.8}$$

where s_0 is the current entropy density. Y_D^0 , which is Y_D at current times, can be gotten using Eqs. (2.15), (4.1), and (4.2), ρ_c is the critical energy density needed to close the Universe, and h is defined so that $H_0=100h~{\rm km\,s^{-1}\,Mpc^{-1}}$, where H_0 is the Hubble parameter today.

The procedure for solving the evolution equations involves simultaneous analysis of coupled equations Eqs. (2.1)–(2.3), (2.15), (B4), and (B5), the yield equations for Y_D , Y'_{γ} , Eqs. (4.1)–(4.2), and Eqs. (4.3)–(4.8). Using these, we do Monte Carlo simulations with parameters varying in the ranges

$$10^{-1} \text{ GeV} < m_D < 10^3 \text{ GeV}, \quad 10^{-2} \text{ MeV} < m_{\gamma'} < 10^2 \text{ MeV}$$

$$10^{-4} < g_X < 1, \quad 10^{-12} < \delta < 10^{-7}, \quad (4.9)$$

TABLE I. Six model points used in the analysis of this work and their decay lifetime for the dark photon.

Mode	1 <i>m</i> _D [GeV]	$m_{\gamma'}$ [MeV]	g_X	$\delta \ ({\rm in} \ 10^{-9})$	$\tau_{\gamma'\to 3\gamma}$ (yrs)
(a)	0.354	0.306	0.00738	3.99	2.6×10^{7}
(b)	0.259	0.214	0.00675	6.29	2.6×10^{8}
(c)	0.281	0.550	0.00931	400	1.3×10^{1}
(d)	0.170	0.225	0.00618	19.3	1.8×10^{7}
(e)	0.156	0.285	0.00631	52.9	2.8×10^{5}
(f)	0.568	0.445	0.00810	2.62	2.0×10^{6}

and search for model points satisfying all the current experimental constraints. Table I gives six model points used in this paper, all of which are consistent with the current experimental constraints [70] including those from a variety of experiments, i.e., BABAR [71,72], HPS [73], LHCb [74], Belle-2 [75], SHiP [76], SeaQuest [77,78] and NA62 [78], CHARM [78], ν Cal [78–80], E137 [81], E141 [82], NA64 [83], NA48 [84]. For a sub-MeV dark photon mass stringent constraints on the parameter space of the model arise from Supernova 338, SN1987A [85] and from BBN, stellar cooling [86] and from the decay to 3γ on cosmological timescales [30,87]. An analysis of these constraints in limiting the parameter space is given in [69,70]. The parameter space chosen in the current analysis is consistent with these constraints.

We note here that the mass of the dark photon is in the sub MeV region and is long lived with its most dominant decay mode being $\gamma' \to 3\gamma$. For kinetic mixing, the decay width for the mode $\gamma' \to 3\gamma$ is given by [30,87,88]

$$\Gamma_{\gamma' \to 3\gamma} = \frac{17\alpha^4 (\epsilon_{\gamma'}^{\gamma})^2 m_{\gamma'}^9}{2^7 3^6 5^3 \pi^3 m_e^8}, \tag{4.10}$$

where $\alpha = \frac{e^2}{4\pi}$, $\epsilon_{\gamma'}^{\gamma}$ is the kinetic mixing parameter of coupling between dark photon γ' and photon γ given by $\epsilon_{\nu'}^{\gamma} = g_Y \sqrt{1 + \bar{\epsilon}^2} \mathcal{R}_{21}$ as defined in [9], $m_{\nu'}$ is the dark photon mass, and m_e is the electron mass. The dark photon lifetimes for the different model points are given in Table I. Here, we find that the dark photon lifetimes are smaller than the age of the Universe, and thus, there is no contribution of the dark photon to the relic density and consequently, no constraint on the allowed parameter space regarding the relic density constraint. We note, however, that even if the dark photon was long lived with a lifetime greater than the lifetime of the Universe, its contribution to the relic density would be negligible. A recent analysis [69] in accord with the analysis of [30] shows that with one hidden sector, it is not possible to get both a long lived dark photon that can contribute to the relic density and simultaneously achieve a significant amount of dark matter relic density. To do that, one needs at least a two hidden sector model [69] in which a dark

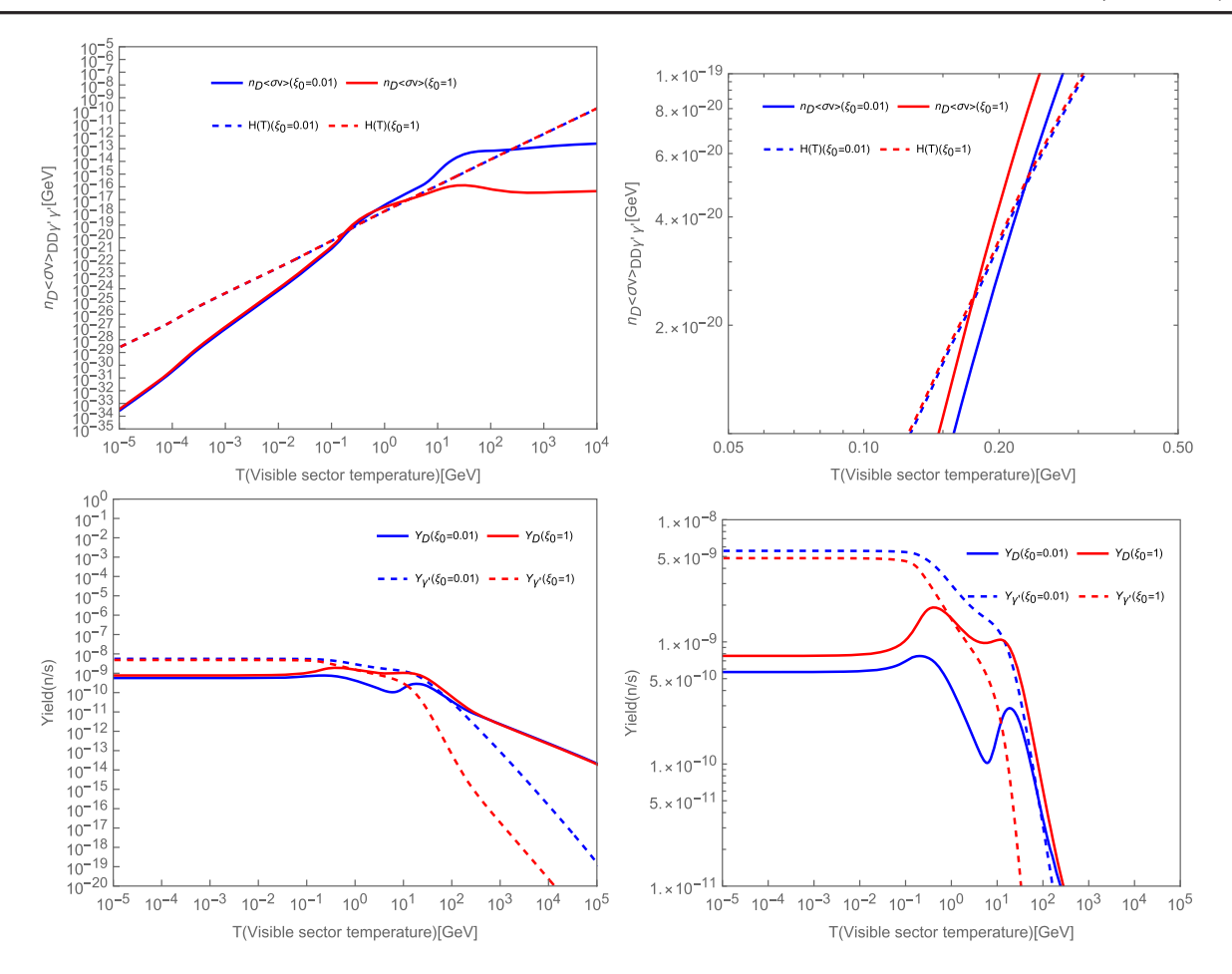


FIG. 1. Top left panel: Exhibition of the dependence of the dark freeze-out temperature when $\xi_0 = 0.01$ (blue) vs $\xi_0 = 1$ (red) for model (f) in Table I. Top right panel: Zoom in of the top left panel in the region of the freeze-out. Bottom left panel: Yields of dark fermion (dark matter) and dark photon for model of the top panels for $\xi_0 = 0.01$ (blue) and $\xi_0 = 1$ (red). Bottom right panel: Zoom in of the bottom left panel to exhibit the shift of the dark fermion yield for the cases $\xi_0 = 0.01$ (blue) and $\xi_0 = 1$ (red).

photon as dark matter can produce a non-negligible amount of dark matter.

We discuss now the dependence of the dark matter freeze-out and of the relic density on the initial conditions. In the top left panel of Fig. 1, we exhibit the dependence of the dark freeze-out and specifically the decoupling of the dark photon and the dark fermion on ξ_0 where we consider the cases: $\xi_0 = 0.01$ and $\xi_0 = 1$. The top right panel is the zoom in of the top right in the region of the freeze-out. From Fig. 1, we see that the process $D\bar{D} \rightarrow \gamma' \gamma'$ falls below H(T) at different temperatures for $\xi_0 = 0.01$ and for $\xi_0 = 1$, and consequently, the temperature where the dark freezeout occurs changes by a significant amount. The sensitivity of the freeze-out on ξ_0 directly affects the yields as shown in the bottom left panel and the bottom right panel (a zoom in of the bottom left panel) of Fig. 1. In the left panel of Fig. 2, we exhibit the dependence of the relic density on ξ_0 for the six model points of Table I. Here, we find that the relic density can change up to 40% as ξ_0 varies in the range (0,1).

B. Dependence of $\Delta N_{\rm eff}$ at BBN on ξ_0

One of the predictions of beyond the standard model physics is $N_{\rm eff}$, the number of effective relativistic degrees of freedom at BBN. For the standard model, $N_{\rm eff}=3.046$. The current experimental constraint on $N_{\rm eff}$ is summarized in Fig. 39 of the Planck Collaboration [89], which shows the spread in $N_{\rm eff}$. Thus, the Planck Collaboration gives $N_{\rm eff}=2.99\pm0.17$, while the joint BBN analysis of deuterium/helium abundance and the Planck CMB data gives $N_{\rm eff}=3.41\pm0.45$. Here, we will use the conservative constraint on $\Delta N_{\rm eff}=N_{\rm eff}^{\rm exp}-N_{\rm eff}^{\rm sm}$ so that $\Delta N_{\rm eff}\leq0.25$. In the model under discussion, the dark fermion D and dark photon γ' will contribute to the effective neutrino number. Such contribution is given by

$$\Delta N_{\text{eff}} = \frac{4}{7} g_{\text{eff}}^h \left(\frac{11}{4}\right)^{4/3} \left(\frac{T_h}{T}\right)^4,$$
 (4.11)

where g_{eff}^h can computed from Eqs. (B4) and (4.11) is to be evaluated at the BBN temperature $T_{\text{BBN}} = 1 \text{ MeV}$

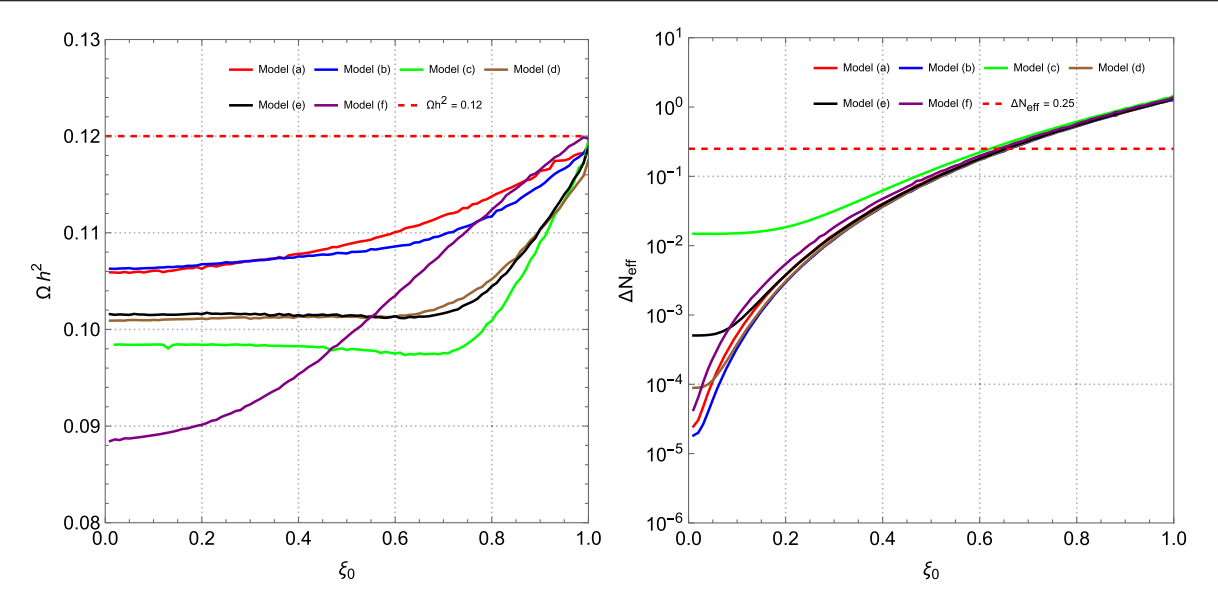


FIG. 2. Left panel: Exhibition of the dependence of the relic density Ωh^2 on ξ_0 in the range $\xi_0 = (0,1)$ for the model points of Table I. Right panel: Exhibition of the dependence of $\Delta N_{\rm eff}$ at BBN time on ξ_0 in the range $\xi_0 = (0,1)$ for the model points of Table I.

(for related works see, e.g., [90,91]). In Table II, $\Delta N_{\rm eff}$ is computed for the six model points of Table I for $\xi_0=0.01$ and $\xi_0=1$, while the right panel of Fig. 2 exhibits $\Delta N_{\rm eff}({\rm BBN})$ for the six model points for ξ_0 in the range (0-1). The analysis in general indicates that hidden sectors which start off cooler than the standard model at the end of reheating contribute a smaller amount to $\Delta N_{\rm eff}$ than those that are relatively hotter at the end of reheating. Further, the analysis indicates that models where $\xi \simeq 0$ could accommodate more massless degrees of freedom allowing for the possibility of building a wider class of models with more hidden sector particles, which may still be consistent with the $\Delta N_{\rm eff}$ constraint at BBN time.

TABLE II. Table of $\Delta N_{\rm eff}$ and $\xi(T_{\rm BBN}) = (T_h/T)_{\rm BBN}$ when $\xi_0 = 0.01$ and $\xi_0 = 1$ for the model points of Table 1. As noted in the text, the benchmarks of this table are chosen to lie in the parameter space allowed in the analysis of Ref. [70], which gives an exhaustive analysis of all of the current experimental constraints on the dark photon and its couplings and exhibits the parameter space still unconstrained.

	$\xi_0 = 1$		$\xi_0 = 0.01$	
Model	$\Delta N_{ m eff}$	$\xi(T_{ m BBN})$	$\Delta N_{ m eff}$	$\xi(T_{ m BBN})$
(a)	1.50	0.692	1.53×10^{-5}	0.0391
(b)	1.36	0.675	1.22×10^{-5}	0.0369
(c)	1.53	0.700	1.18×10^{-2}	0.208
(d)	1.40	0.679	6.37×10^{-5}	0.0558
(e)	1.43	0.684	3.80×10^{-4}	0.0873
(f)	1.42	0.685	2.59×10^{-5}	0.0448

C. Effect of ξ_0 on the allowed parameter space and on spin-independent proton-DM cross section

Next, we investigate the influence of ξ_0 on the allowed parameter space consistent for a chosen range of relic density. To this end, we constrain the relic density to lie in the range $0.012 < \Omega h^2 < 0.12$ and m_D to lie in the range of 5 GeV to 10 TeV. Specifically, we explore the allowed region for the two cases: $\xi_0 = 0.01$ and $\xi_0 = 1$. The result of our analysis is exhibited in the left panel of Fig. 3, which gives a scatter plot of the allowed models in δ vs $m_{\nu'}$, where those with color blue correspond to $\xi_0 = 0.01$ and those with color red correspond to $\xi_0 = 1$. One of the interesting result that emerges is that for $\xi_0 = 1$, most of the models lie in the range $10^{-10} < \delta < 10^{-5}$, while for $\xi_0 = 0.01$, the allowed range is $10^{-9} < \delta < 10^{-4}$. Thus, the analysis shows that the initial choice of ξ_0 significantly impacts the model's allowed parameter space. ξ_0 also has significant effect on the proton-DM scattering cross section in the direct detection experiments for dark matter. Specifically, we consider the spin-independent proton-DM cross section $\sigma_{\text{SI:p-DM}}$. Here, we use the micrOMEGAs [4] to find the spin independent cross section. In the right panel of Fig. 3, we exhibit $\sigma_{\rm SI:p-DM}$ for the six model points of Table I, and their dependence on ξ_0 in the range (0.01–1) is indicated by the small vertical lines for each of the model points. The numerical values of the $\sigma_{\mathrm{SI:p-DM}}$ for $\xi_0=0.01$ and $\xi_0=1$ are exhibited in Table III for the models of Table I. Here, one finds that the variation of the cross section can be as large as 40%. Thus, some of the models that are eliminated for the $\xi_0 = 1$ case would still be viable for the case $\xi_0 = 0.01$.

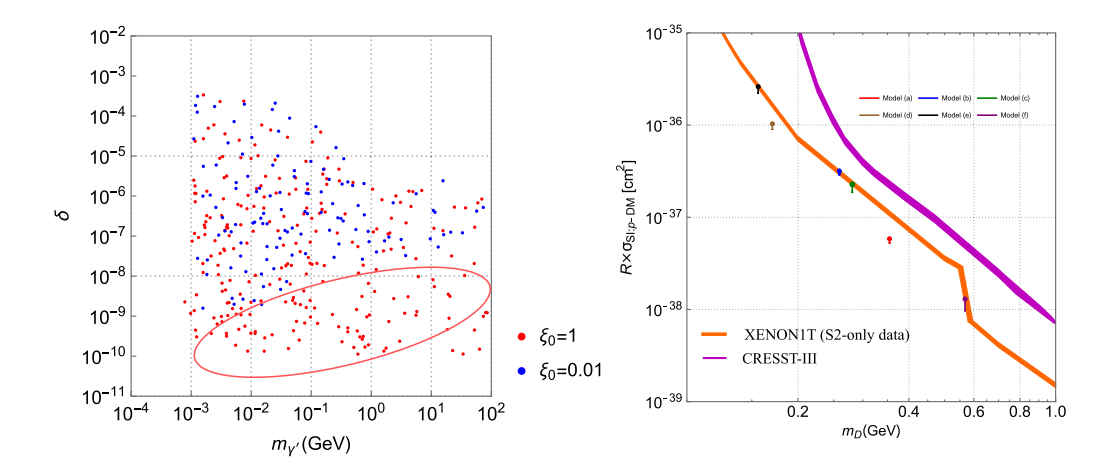


FIG. 3. Left panel: A scatter plot of δ vs m_{γ} displaying the models allowed under the constraint $0.012 \le \Omega h^2 \le 0.12$ for $\xi_0 = 0.01$ (blue) and $\xi_0 = 1$ (red). The solid red ellipse shows that a significant region of the parameter space in the $m_{\gamma}' - \delta$ plane becomes accessible when $\xi_0 = 1$, which would otherwise be excluded when $\xi = 0.01$. This is meant as an illustration that ξ_0 plays a significant role in determining the allowed parameter space of models. Right panel: Plot of the spin-independent proton-DM cross section for six model points where the vertical lines show the shift in the cross section as one moves from $\xi_0 = 0.01$ to $\xi_0 = 1$. The experiment constraints are from CRESST-III [92] and XENONIT [93].

V. SELF-INTERACTING DARK MATTER, SOMMERFELD ENHANCEMENT, AND DEPENDENCE ON ξ_0

The self-interacting dark matter cross sections arises from the processes $D\bar{D} \to D\bar{D}$, $DD \to DD$ and $\bar{D}\bar{D} \to \bar{D}\bar{D}$ via the exchange of a dark photon. The Lagrangian of Eq. (3.1) leads to a Yukawa potential between the D fermions due to the dark photon exchange in the non-relativistic limit so that

$$V(\vec{r}) = \pm \frac{(g_X)^2}{4\pi} \frac{e^{-m_{\gamma'}r}}{r},$$
 (5.1)

where the plus sign is for $DD \to DD$ and $\bar{D}\bar{D} \to \bar{D}\bar{D}$ and the minus sign is for $D\bar{D} \to D\bar{D}$. In some of the regions of parameters (i.e., $\frac{m_{\gamma'}}{m_D} \le \frac{(g_X)^2}{4\pi}$), tree-level scattering or the Born approximation is no longer valid, and one has contributions from higher order dark photon exchanges as shown in Fig. 4, which contribute to scattering. In this

TABLE III. Table of spin-independent proton-DM cross section $\sigma_{\text{SI:p-DM}}$ for the model points of Table 1 for $\xi_0=0.01$ and $\xi_0=1.0$.

	$\xi_0 = 1$	$\xi_0 = 0.01$
Model	$\sigma_{\rm SI:p-DM}~({\rm cm}^2)$	$\sigma_{\rm SI:p-DM}~({\rm cm}^2)$
(a)	5.84×10^{-38}	5.24×10^{-38}
(b)	3.18×10^{-37}	2.87×10^{-37}
(c)	2.19×10^{-37}	1.81×10^{-37}
(d)	1.03×10^{-36}	8.88×10^{-37}
(e)	2.61×10^{-36}	2.23×10^{-36}
(f)	1.39×10^{-38}	1.03×10^{-38}

case, we need to numerically solve the Schrodinger equation to find the accurate scattering cross sections. The radial equation one needs to solve is given by

$$\left(\frac{d^2R_l}{dr^2} + \frac{2}{r}\frac{dR_l}{dr} - \frac{l(l+1)R_l}{r^2}\right) + (p^2 - 2\mu V(r))R_l = 0,$$
(5.2)

where p is the particle momentum, and V(r) is the potential. The substitution x = pr and $R_{p,l} = Np\Phi_l(x)/x$ gives [94]

$$\left(\frac{d^2}{dx^2} + 1 - \frac{l(l+1)}{x^2} - \frac{2ae^{-bx}}{x}\right) \Phi_l(x) = 0,$$

$$a = \pm \frac{\mu g_X^2}{4\pi p}, \qquad b = \frac{m_{\gamma'}}{p}.$$
(5.3)

The nonperturbative effect arising from the repeated exchange of the mediator is often encoded in Sommerfeld enhancement and has been discussed in several previous works (see, e.g., [24,36,95-98] and the references therein). Thus, including nonperturbative effects, the annihilation cross section times the velocity v (where v is the relative

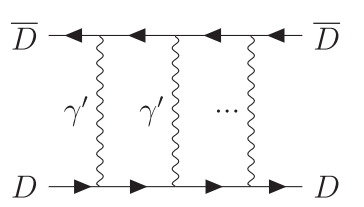


FIG. 4. A diagram exhibiting a contribution to $D\bar{D} \to D\bar{D}$ scattering beyond the Born approximation.

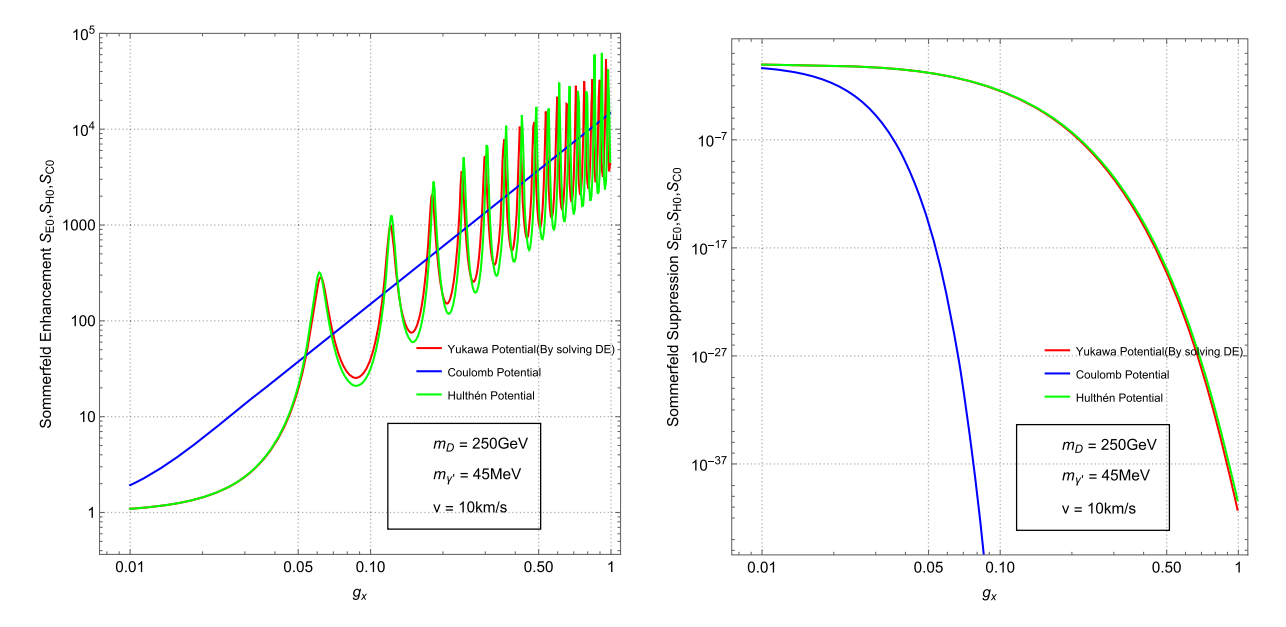


FIG. 5. Left panel: Plot of S wave Sommerfeld enhancement for an attractive potential, where S_{E0} is for the Yukawa potential by solving numerically (red), S_{C0} is for the Coulomb potential (black), and S_{H0} is for the Hulthen potential as a function of g_X for the case when $m_D = 250$ GeV, $m_{\gamma'} = 45$ MeV, and v = 10 km/s. Right panel: Plot of S wave Sommerfeld suppression for the case of a repulsive potential where we use the same symbols S_{E0} , S_{H0} , S_{C0} for suppression as for enhancement to avoid a proliferation of notation.

velocity in the CM system) for the cross section σ_{ab} for the elastic scattering process $a + b \rightarrow a + b$ may be written as

$$(\sigma_{ab}v) = S_E(\sigma_{ab}^0v), \tag{5.4}$$

where $(\sigma_{ab}^0 v)$ is the tree-level cross section, and S_E is the Sommerfeld enhancement. As noted in the present context, the contribution to the Sommerfeld enhancement arises from multiple exchanges of the dark photon γ' . The solution of the differential equation Eq. (5.3) has the form:

$$\Phi_l(x)_{x\to\infty} \to A \sin\left(x - \frac{l\pi}{2} + \delta_l\right),$$
(5.5)

where δ_l is the phase shift for the *l*th partial wave. We write the Sommerfeld enhancement of *l*th partial wave cross section for the case of the Yukawa potential so that

$$\sigma_I = S_{FI} \cdot \sigma_{0I}, \tag{5.6}$$

where [94], $S_{El} = (1 \cdot 3 \cdots (2l+1)/A)^2$. Using Eq. (5.5), we get

$$A^{2} = A^{2} \sin^{2}\left(x - \frac{l\pi}{2} + \delta_{l}\right) + A^{2} \cos^{2}\left(x - \frac{l\pi}{2} + \delta_{l}\right)$$

$$= \Phi_{l}^{2}(x)_{x \to \infty} + \Phi_{l}^{2}\left(x - \frac{\pi}{2}\right)_{x \to \infty},$$

$$S_{El} = \frac{((2l+1)!!)^{2}}{\Phi_{l}^{2}(x)_{x \to \infty} + \Phi_{l}^{2}(x - \frac{\pi}{2})_{x \to \infty}}.$$
(5.7)

Taking x larger than 30 gives a good enough approximation to the exact solution. Typically, an attractive potential leads to Sommerfeld enhancement of cross section at low collision velocities, but one may also have Sommerfeld suppression for a repulsive potential. In the left panel of Fig. 5, we exhibit Sommerfeld enhancement for the case of a negative Yukawa potential. Here, we see that Sommerfeld enhancement can be very significant, and further, the enhancement shows oscillatory behavior with g_X . To check the accuracy of our numerical analysis and to explain the oscillatory behavior, we compare our result with those from the Hulthen potential as an approximation to the Yukawa potential for which one can obtain a good analytic approximation for the S wave. The Hulthen potential is given by [99,100]

$$V(r) = -\alpha \frac{\mu e^{-\mu r}}{1 - e^{-\mu r}}, \quad \mu = \frac{\pi^2 m_{\gamma'}}{6}, \quad \alpha = \frac{(g_X)^2}{4\pi}.$$
 (5.8)

It is known that Hulthen potential is a very good approximation to Yukawa potential both at short and at long distances. With it, one can find an analytic solution for the *S* wave and thus, find a good analytic approximation to the *S* wave Sommerfeld enhancement [101,102]:

$$S_{H0} = \frac{\pi}{\epsilon_v} \frac{\sinh(2\pi\epsilon_v \beta)}{\cosh(2\pi\epsilon_v \beta) - \cos(2\pi\sqrt{\beta - \epsilon_v^2 \beta^2})},$$

$$\epsilon_v = \frac{v}{2\alpha}, \qquad \epsilon_x = \frac{m_{\gamma'}}{\alpha m_D}, \qquad \beta = \frac{1}{\pi^2 \epsilon_v / 6}.$$
(5.9)

From Eq. (5.9), valid for the attractive potential case, it is obvious that the oscillation is due to the existence of the cosine term. For the Coulomb potential, the Sommerfeld enhancement for the S wave is given by

$$S_{C0} = \pm \frac{2\pi\alpha}{v} \frac{1}{e^{\pm 2\pi\alpha/v} - 1}$$
 (5.10)

where plus is for repulsive potential and minus is for attractive potential. The left panel of Fig. 5 gives a comparison of the S wave Sommerfeld effect for three different potentials: Yukawa, Hulthen, and Coulomb. The analysis shows that Hulthen potential gives a good approximation to the Yukawa potential and also explains the deep oscillations as a function of g_X . For the case of a repulsive potential (α negative), the analysis is very different. A comparison of the numerical analysis using Yukawa potential and the analytic solution using Hulthen potential for the case of a repulsive potential is given in the right panel of Fig. 5. Here again, one finds that the numerical analysis and the Hulthen potential result fully agree.

Having checked the numerical accuracy of our analysis in Fig. 5, we next investigate the effect of the big bang initial conditions on Sommerfeld enhancement. In Fig. 6, we compare S wave Sommefeld enhancement for the cases $\xi_0=0.01$ and $\xi_0=1$ for the case of an attractive Yukawa potential. The left panel of Fig. 6 shows Sommmerfeld enhancement vs v, and here, one finds that $\xi_0=1$ (red) gives an enhancement which is larger than for the case $\xi_0=0.01$ (blue). In the analysis, we keep the relic density fixed at ~ 0.12 for $\xi_0=0.01$ and $\xi_0=1$ by allowing g_X to vary. The right panel of Fig. 6 displays Sommerfeld

enhancement as a function of $m_{\gamma'}/m_D$, and here, one finds that the oscillation peaks for the case $\xi_0=1$ (red) are significantly larger than those for the case $\xi_0=0.01$ (blue). A similar analysis for a repulsive Yukawa potential is carried out in Fig. 7. However, in this case, we have Sommerfeld suppression rather than an enhancement where the Sommerfeld suppression is vs v for the left panel and vs $m_{\gamma'}/m_D$ for the right panel, and the red curve is for $\xi_0=1.0$ and the blue curve for $\xi_0=0.01$. For both cases, the Sommerfeld suppression is significantly larger for $\xi_0=1$ relative to $\xi_0=0.01$.

VI. EFFECT OF ξ_0 ON FIT TO GALAXY DATA

Several analyses of galaxy data indicate that dark matter is collisional at the scale of dwarf galaxies and appears collisionless at the scale of galaxy clusters [33,38,103]. Thus, for dwarf galaxies, one finds collisional velocity $\langle v \rangle$ of dark matter in the range 10-100 km/s and $1 \text{ cm}^2/\text{g} < 10$ $\sigma/m < 50 \text{ cm}^2/\text{g}$ [33,103], where σ is the cross section, and m is the mass of DM particle. For midsize galaxies such as the low surface brightness galaxies (LSB) and the Milky Way, one finds $\langle v \rangle$ in the range 80–200 km/s and $0.5 \text{ cm}^2/\text{g} < \sigma/m < 5 \text{ cm}^2/\text{g}$. The galaxy clusters exhibit $\langle v \rangle > 1000$ km/s. Here, it is estimated that the σ/m is maximally $1 \text{ cm}^2/\text{g}$ [33,103,104] and could be as low as $0.065 \text{ cm}^2/\text{g} < \sigma/m < 1 \text{ cm}^2/\text{g}$ [38,105,106]. As is well known, one interesting possibility to account for the velocity dependence of the DM cross sections is that DM is self-interacting by Spergel and Steinhardt [107], and there is considerable follow up work on this idea [22,25–28,36,108–115]. An analysis of fit to the data

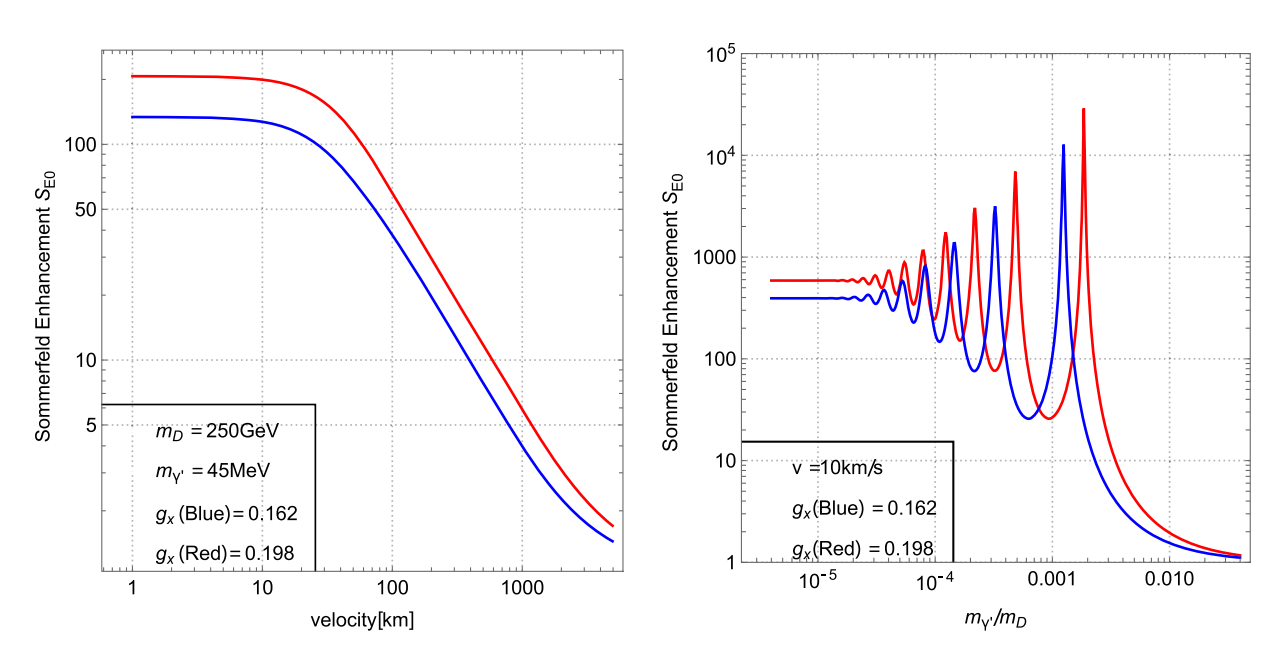


FIG. 6. Plot of *S* wave Sommerfeld enhancement for an attractive Yukawa potential for the case $\xi_0 = 0.01$ (blue) and for $\xi_0 = 1$ (red), where for the left panel, the *x* axis is *v*, and for the right panel, the *x* axis is $m_{\gamma'}/m_D$. Here, we allow g_X to vary but keep the relic density ~ 0.12 for $\xi_0 = 0.01$ and $\xi_0 = 1$.

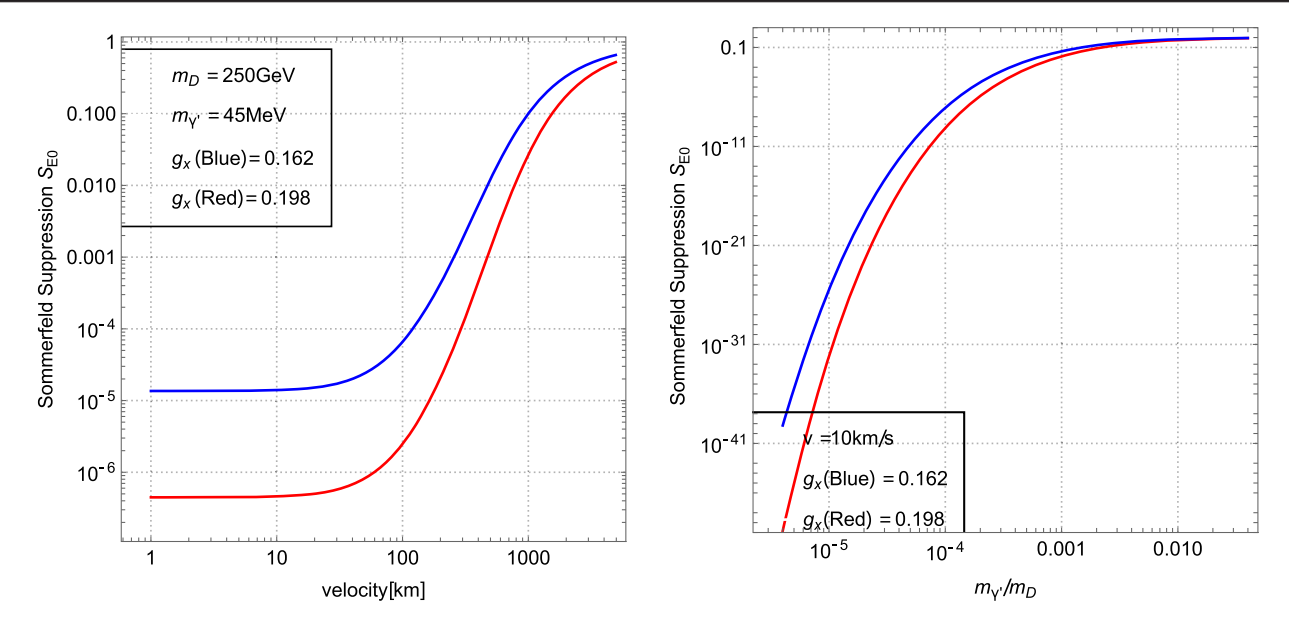


FIG. 7. Plot of *S* wave Sommerfeld suppression for a repulsive Yukawa potential for the case $\xi_0 = 0.01$ (blue) and for $\xi_0 = 1$ (red), where for the left panel, the *x* axis is v, and for the right panel, the *x* axis is $m_{\gamma'}/m_D$. Here, we allow g_X to vary to keep the relic density ~ 0.12 for $\xi_0 = 0.01$ and for $\xi_0 = 1$.

within the dark photon model was previously done in [11] (see also [116,117]). Here, we study the dependence of the fits on ξ_0 . Further, here, the analysis goes beyond the Born approximation used in [11], taking into account nonperturbative effects encoded in the Sommerfeld enhancement with also inclusion of identical particle exchange effects. Since the dark matter is constituted of dark Dirac fermions consisting of D and \bar{D} constituents, we will have processes of the type $DD \to DD$, $D\bar{D} \to D\bar{D}$, and $\bar{D}\bar{D} \to \bar{D}\bar{D}$. Thus, the total cross section $\sigma_{\rm DM}$ is given by

$$\sigma_{\rm DM} = \int d\Omega \bigg[\frac{d\sigma_{D\bar{D}\to D\bar{D}}}{d\Omega} + \frac{1}{2} \frac{d\sigma_{D\bar{D}\to D\bar{D}}}{d\Omega} + \frac{1}{2} \frac{d\sigma_{\bar{D}\bar{D}\to \bar{D}\bar{D}}}{d\Omega} \bigg], \tag{6.1}$$

where the factor of 1/2 arises due to identical nature of particles.

To numerically calculate the cross section, we start with Eq. (5.3) and use the method of [27]. Here, in the computation of DM cross sections, we need to calculate the phase shifts (δ_ℓ) for $D\bar{D}\to D\bar{D}$ separately from the phase shifts (δ'_ℓ) for $DD\to DD$, while the phase shifts for the process $\bar{D}\bar{D}\to \bar{D}\bar{D}$ will be the same as for the process $DD\to DD$. Including all contributions, i.e., from $D\bar{D}\to D\bar{D}$, $DD\to DD$, and $\bar{D}\bar{D}\to D\bar{D}$, and taking account of the identical nature of particles in $DD\to DD$ and $\bar{D}\bar{D}\to D\bar{D}$ scattering, we find

$$\sigma_{\text{tot}} = 4\pi \sum_{\ell} (2\ell + 1) \left[|f_{\ell}|^2 + 2\left(1 - \frac{1}{2}(-1)^{\ell}\right) |f_{\ell}'|^2 \right],$$
(6.2)

where $f_\ell = e^{i\delta_\ell} \sin \delta_\ell/k$ and $f'_\ell = e^{i\delta'_\ell} \sin \delta'_\ell/k$. The details leading to Eq. (6.2) are given in Appendix C. The result of our numerical analysis to fit the galaxy data on $\sigma v/m_D$ in the range of velocities from 10 km/s to 10⁴ km/s is given in Fig. 8, which exhibits the dependence of the fits on ξ_0 in the range $\xi_0 = 0.01$ to $\xi_0 = 1$. In the analysis, we allow g_X to vary to keep the relic density fixed at $\Omega_D h^2 \sim 0.12$ as ξ_0 varies between 0.01 and 1. The analysis shows that the variation of $\sigma v/m$ with ξ_0 is significant and can sometimes be as large as O(1) [see Model (f)] in Fig. 8. We note that the plots include Sommerfeld enhancement effects, but these effects are relatively small. The reason for it is that the Sommerfeld enhancement strongly depends on g_X as can be seen from the left panel of Fig. 5. However, in the analysis of galaxy fits of Fig. 8, we find that g_X is relatively small, which suppresses the Sommerfeld enhancement. Our result here is consistent with a similar observation on Sommerfeld enhancement in the work of [36] (see also [24]). In Fig. 8, the Born approximation results are also plotted for comparison with the exact solutions. Further, we note that more fine tuned fits to the galaxy data can be gotten by adjustment of the model parameters such that resonances appear in some of the low lying partial waves, e.g., S, P, and D waves. This is exhibited in Fig. 9, where in the left panel, we see enhancements in the S and the P waves appear to simulate the oscillations in the data at $\langle v \rangle \sim$ 10^2 km/s and at $\langle v \rangle \sim 10^3$ km/s. On the right panel of Fig. 9, we plot the cross section contributed from each partial wave separately. It is clear that the peak at $\langle v \rangle \sim$ 10^2 km/s is largely due to the S wave while the one at $\langle v \rangle \sim 10^3$ km/s has a large contribution from l = 5,

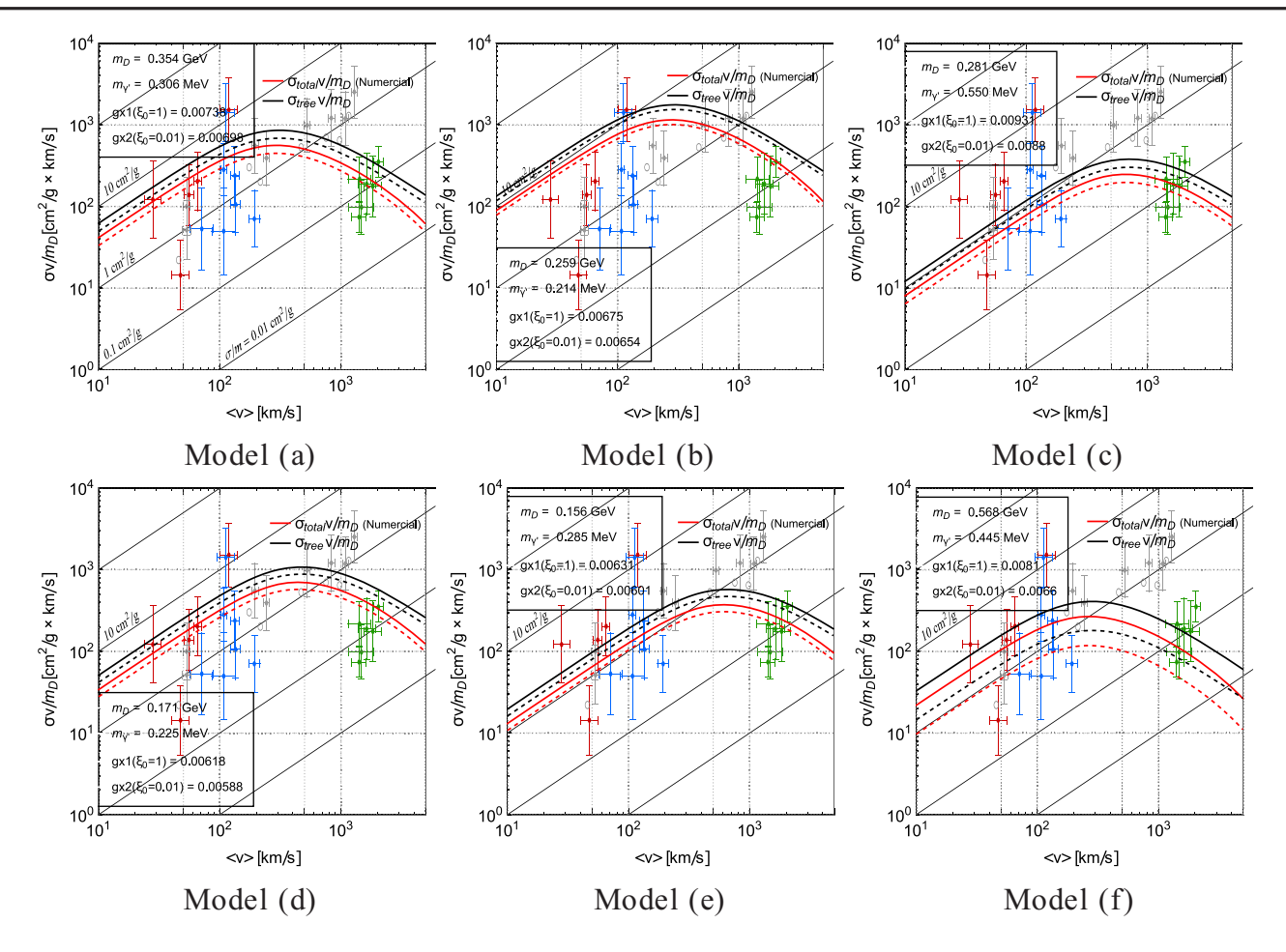


FIG. 8. A fit to the galaxy data taken from [33], which studies the dependence of $\sigma v/m_D$ on ξ_0 in the range (0.01–1) for the six models of Table 1. Here, solid lines are for $\xi_0 = 1$ and the dashed line for $\xi_0 = 0.01$ exhibit the dependence of $\sigma v/m_D$ on ξ_0 . The fits (in red) are done using the full analysis by numerically integrating the Schrodinger equation including identical particle effects as well as Sommerfeld enhancement. For comparison, we also exhibit the tree-level QFT cross section shown by black curves that does not consider the effect of identical scattering. In the analysis, we allow g_X to vary but keep the relic density fixed at ~0.12 as ξ_0 varies. It is to be noted that "galaxy data" is itself a computed quantity based on observation as evident from [33].

although the sum of all partial waves up to l = 5 enter in the fit given on the left panel.

Besides the total cross section, the transfer cross section [22,23,25–28,118] σ_T has been used in simulations of long range interactions [108,111,119]. Further, the viscosity cross section σ_V is also widely used in analyses of SIDM [27,120,121]. They are defined so that

$$\sigma_{\text{total}} = \int \frac{d\sigma}{d\Omega} d\Omega,$$

$$\sigma_T = \int \frac{d\sigma}{d\Omega} (1 - \cos\theta) d\Omega,$$

$$\sigma_V = \int \frac{d\sigma}{d\Omega} (1 - \cos^2\theta) d\Omega.$$
 (6.3)

In terms of partial waves, σ_T and σ_V are given by

$$\sigma_{\rm T} = 4\pi \sum_{\ell} \left[T(f_{\ell}) + 2\left(1 - \frac{1}{2}(-1)^{\ell}\right) T(f_{\ell}') \right], \quad (6.4)$$

$$\sigma_{V} = 4\pi \sum_{\ell} \left[V(f_{\ell}) + 2\left(1 - \frac{1}{2}(-1)^{\ell}\right) V(f'_{\ell}) \right], \quad (6.5)$$

$$T(f_{\ell}) = ((2l+1)|f_{l}|^{2} - lf_{l}f_{l-1}^{*} - (l+1)f_{l}f_{l+1}^{*}), \quad (6.6)$$

$$V(f_{\ell}) = \left(\frac{2(l^{2} + l - 1)(2l + 1)}{(2l - 1)(2l + 3)}|f_{l}|^{2} - \frac{(l - 1)l}{(2l - 1)}f_{l}f_{l-2}^{*} - \frac{(l + 2)(l + 1)}{(2l + 3)}f_{l}f_{l+2}^{*}\right).$$

$$(6.7)$$

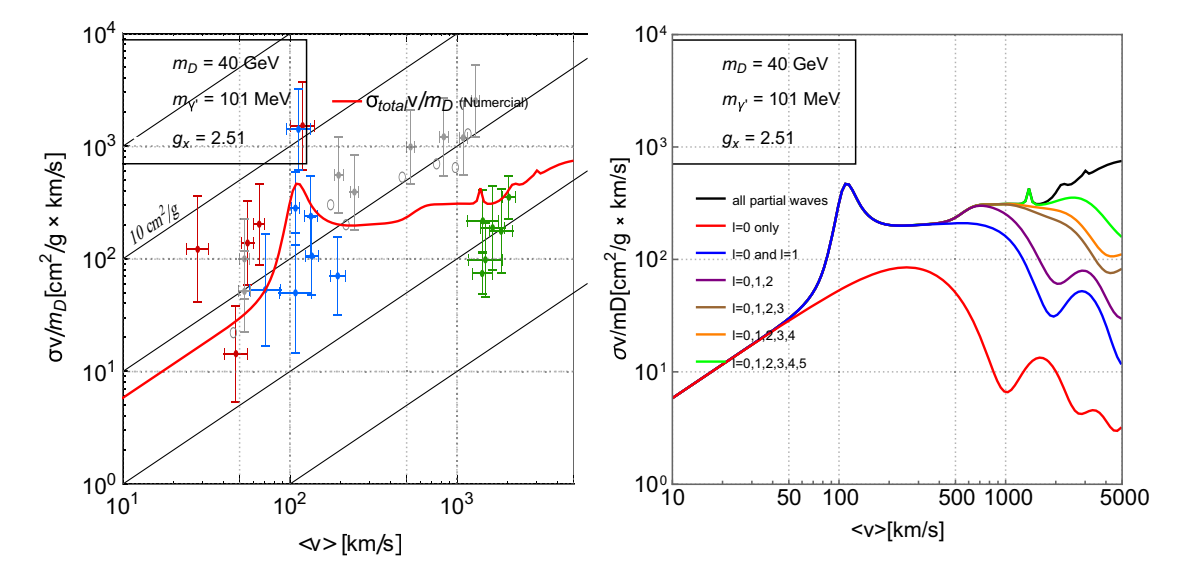


FIG. 9. Left: Exhibition of peaks in fits to the galaxy data (which is the same as in Fig. 8) with specific parameters. Right panel: Here, it is shown how the peaks in the left panel at $\langle v \rangle \sim 10^2$ km/s and at $\langle v \rangle \sim 10^3$ km/s arise from successive additional of higher waves. Thus, the peak at $\langle v \rangle \sim 10^2$ km/s arises mainly from S and P contributions, while the one at $\langle v \rangle \sim 10^3$ km/s arises from contributions from up to l=5.

Details of their computation in terms of partial waves are given in Appendix C. Figure 10 shows that σ_{tot} , σ_T , σ_V differ significantly from each other. We also exhibit the tree-level cross section for comparison.

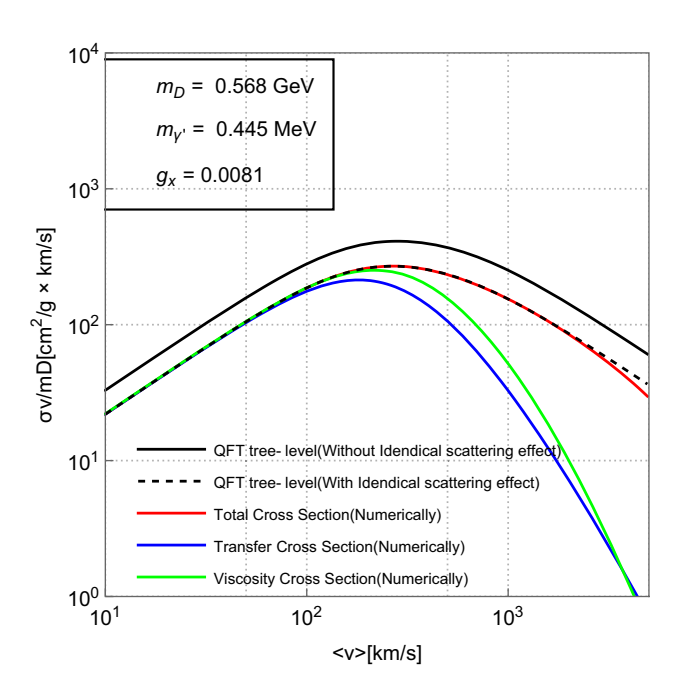


FIG. 10. A comparison of $\sigma v/m_D$ vs v for different cross sections, which include the total cross section $\sigma_{\rm total}$, the transverse cross section σ_T , the viscosity cross section σ_V as defined by Eq. (6.3) and the tree-level QFT cross section with and without identical particle effects for model (f) of Table I. The analysis is done for $\xi_0 = 1$.

VII. CONCLUSION

Hidden sectors are ubiquitous in models of extra dimensions, in extended supergravity, and in strings and appear in a variety of beyond the standard model constructions such as in moose/quiver gauge theories (see, e.g., [122–125]). While the hidden sectors are neutral under the standard model gauge group, they can couple feebly with the standard model. However, the couplings of the hidden sector to the inflaton could vary over a wide range. Thus, on one extreme, the hidden sector coupling to the inflaton could be negligible relative to the coupling of the standard model. In this case, at the end of reheating, there would be essentially no production of the hidden sector particles, except via gravitational production, and the hidden sector would likely be colder than the standard model. On the other extreme, the hidden sector and the visible sectors could couple democratically to the inflaton, and in this case, the hidden sector and the visible sectors would be in thermal equilibrium at the end of reheating. These two extremes would have significantly different thermal evolution and would result in significant differences in their predictions of the physical observables. In this work, we have investigated these effects in the context of a specific hidden sector model, which arises from a $U(1)_X$ extension of the standard model gauge group. The contents of the hidden sector consists of a dark fermion, which has gauge interactions with the $U(1)_X$ gauge field. The communication between the hidden sector and the visible sector arises from kinetic mixing between the $U(1)_X$ and $U(1)_Y$ gauge fields, where the $U(1)_X$ gauge field acquires mass via the Stueckelberg mechanism. In view of the asymmetric coupling of the visible and the hidden sectors to the inflaton field, the temperature of the hidden sector T_h^0 and of the visible sector T^0 will, in general, be unequal at the end of reheating. Thus, the ratio of the two, i.e., $\xi_0 = (T_h^0/T^0)$, enters in the thermal evolution of the hidden and the visible sectors and affects phenomena at low energy.

The analysis of the work provides a cosmologically consistent framework in that it involves a synchronous evolution of the coupled hidden and visible sectors. In the above framework, we investigate a number of phenomena and their dependence on ξ_0 . These include dark freeze-out, relic density, and the extra number of relativistic degrees of freedom at the BBN time, and the proton-DM cross section. Further, we investigate the effects of ξ_0 on the selfinteraction cross section and on Sommerfeld enhancement. The model is then used in fitting self-interacting dark matter cross sections from galaxy scales to the scale of galaxy clusters. Here, we find that fits to data show a significant variation sometime as much as O(1) for ξ_0 in the range (0,1). Thus, the analysis indicates that inclusion of hidden sectors that appear in a variety of models of particle physics beyond the standard model and the initial constraints on the hidden sector at the end of reheating and specifically on ξ_0 could have significant influence on observables, and thus, their inclusion will be relevant for accurate description of physical phenomena. While our analysis is done for the case of one portal, the general techniques discussed here would be valid for a broader class of models. Finally, we show that the approximation often made in the thermal evolution of visible and hidden sectors by assuming entropy conservation for each of the sectors separately gives widely inaccurate results even for the case for very feeble interactions such as, for example, with the kinetic mixing parameter as low as $\delta = 10^{-10}$. Such an analysis is thus a poor approximation to the analysis we carry out for the thermal evolution of the visible and the hidden sectors in a synchronous manner using Eq. (2.15). For generality, we also consider the case with the mass mixing parameter ϵ that reaches a similar conclusion. We have also analyzed the accuracy of assuming the conservation of total entropy for the yield equations and find that the differences between conservation assumption and no conservation assumption are typically within O(15%). We conclude that an accurate thermal evolution is essential for the current and future precision analyses in cosmology while analyzing physics involving hidden sectors.

ACKNOWLEDGMENTS

Discussions with Amin Abou Ibrahim and Zhuyao Wang are acknowledged. The research of J. L. and P. N. was supported in part by the NSF Grant No. PHY-2209903.

APPENDIX A: SOURCE FUNCTIONS

The source term j_h that appears in Eq. (2.15) is defined by:

$$j_h = \sum_i [2Y_i^{\rm eq}(T)^2 J(i\bar{i} \to D\bar{D})(T) + Y_i^{\rm eq}(T)^2 J(i\bar{i} \to \gamma')(T)] s^2 - Y_{\gamma'} J(\gamma' \to e^+ e^-)(T_h) s. \tag{A1}$$

The J functions that appear in Eq. (A1) are defined as

$$\begin{split} n_i^{\rm eq}(T)^2 J(i\bar{i} \to D\bar{D})(T) \\ &= \frac{T}{32\pi^4} \int_{s_0}^{\infty} ds \sigma_{D\bar{D} \to i\bar{i}} s(s-s_0) K_2(\sqrt{s}/T), \quad \ ({\rm A2}) \end{split}$$

$$n_i^{\text{eq}}(T)^2 J(i\bar{i} \to \gamma')(T)$$

$$= \frac{T}{32\pi^4} \int_{s_0}^{\infty} ds \sigma_{i\bar{i} \to \gamma'} s(s - s_0) K_2(\sqrt{s}/T), \quad (A3)$$

$$n_{\gamma'}J(\gamma'\to e^+e^-)(T_h)=n_{\gamma'}m_{\gamma'}\Gamma_{\gamma'\to e^+e^-}, \eqno({\rm A4})$$

and

$$n_i^{\text{eq}}(T)^2 \langle \sigma v \rangle_{i\bar{i} \to \gamma'}(T)$$

$$= \frac{T}{32\pi^4} \int_{s_0}^{\infty} ds \sigma(s) \sqrt{s} (s - s_0) K_1(\sqrt{s}/T), \quad (A5)$$

where, as noted earlier, K_1 is the modified Bessel function of the second kind and degree one, and s_0 is the minimum value of the Mandelstam variable s.

APPENDIX B: MODEL DETAILS

In addition to the interactions given in Sec. III, there are interactions involving the dark sector and the standard model particles in the canonical basis where the kinetic energy and the mass matrices of the gauge boson are diagonal. Here, the standard model fermions (i.e., quarks and leptons) have feeble interactions with the dark photon, which are given by

$$\Delta \mathcal{L}_{\text{int}} = \frac{g_2}{2\cos\theta} \bar{\psi}_f \gamma^{\mu} [(v'_f - \gamma_5 a'_f) A^{\gamma'}_{\mu}] \psi_f, \quad (B1)$$

where g_2 is the $SU(2)_L$ gauge coupling constant, f stands for the standard model fermions, and angle θ is defined in Eq. (B3). The vector and axial vector couplings of the dark photon with the SM fermions f are given by

$$v'_{f} = -\cos\psi[(\tan\psi - s_{\delta}\sin\theta)T_{3f} - 2\sin^{2}\theta(-s_{\delta}\csc\theta + \tan\psi)Q_{f}],$$

$$a'_{f} = -\cos\psi(\tan\psi - s_{\delta}\sin\theta)T_{3f}.$$
(B2)

Here, $s_{\delta} = \sinh \delta$, T_{3f} is the third component of isospin, and Q_f is the electric charge for the fermion f. The angles θ and ψ , which, along with ϕ , are the three Euler angles with diagonalize the 3×3 gauge boson mass square matrix involving the fields C^{μ} , B^{μ} , A_3^{μ} , are defined as [9]

$$\tan \phi = -s_{\delta}, \qquad \tan \theta = \frac{g_Y}{g_2} c_{\delta} \cos \phi, \qquad \tan 2\psi = \frac{-2s_{\delta} m_Z^2 \sin \theta}{m_{\gamma'}^2 - m_Z^2 + (m_{\gamma'}^2 + m_Z^2 - m_W^2)\delta^2}, \tag{B3}$$

where $c_{\delta} = \cosh \delta$. For the model of Eq. (3.1), where the hidden sector consists of the dark photon and a dark Dirac fermion, g_{eff}^h and h_{eff}^h are given by

$$g_{\text{eff}}^{h} = g_{\text{eff}}^{\gamma'} + g_{\text{eff}}^{D}, \qquad h_{\text{eff}}^{h} = h_{\text{eff}}^{\gamma'} + h_{\text{eff}}^{D},$$

$$g_{\text{eff}}^{\gamma'} = \frac{45}{\pi^4} \int_{x_{\gamma}^{\prime}}^{\infty} \frac{\sqrt{x^2 - x_{\gamma}^2}}{e^x - 1} x^2 dx, \qquad h_{\text{eff}}^{\gamma'} = \frac{45}{4\pi^4} \int_{x_{\gamma}^{\prime}}^{\infty} \frac{\sqrt{x^2 - x_{\gamma}^2}}{e^x - 1} (4x^2 - x_{\gamma}^2) dx,$$

$$g_{\text{eff}}^{D} = \frac{60}{\pi^4} \int_{x_D}^{\infty} \frac{\sqrt{x^2 - x_D^2}}{e^x + 1} x^2 dx, \qquad h_{\text{eff}}^{D} = \frac{15}{\pi^4} \int_{x_D}^{\infty} \frac{\sqrt{x^2 - x_D^2}}{e^x + 1} (4x^2 - x_D^2) dx,$$
(B4)

where $x_D = m_D/T_h$, $x_{\gamma'} = m_{\gamma'}/T_h$.

Further, to compute $\zeta_h = \frac{3}{4}(1 + \frac{p_h}{\rho_h})$, we need ρ_h and p_h , which are given by

$$\rho_{h} = \rho_{\gamma'} + \rho_{D}, \qquad p_{h} = p_{\gamma'} + p_{D},
\rho_{\gamma'} = \frac{g_{\gamma'} T^{4}}{2\pi^{2}} \int_{x_{\gamma'}}^{\infty} \frac{\sqrt{x^{2} - x_{\gamma'}^{2}}}{e^{x} - 1} x^{2} dx, \qquad p_{\gamma'} = \frac{g_{\gamma'} T^{4}}{6\pi^{2}} \int_{x_{\gamma'}}^{\infty} \frac{(x^{2} - x_{\gamma'}^{2})^{\frac{3}{2}}}{e^{x} - 1} dx,
\rho_{D} = \frac{g_{D} T^{4}}{2\pi^{2}} \int_{x_{D}}^{\infty} \frac{\sqrt{x^{2} - x_{D}^{2}}}{e^{x} + 1} x^{2} dx, \qquad p_{D} = \frac{g_{D} T^{4}}{6\pi^{2}} \int_{x_{D}}^{\infty} \frac{(x^{2} - x_{D}^{2})^{\frac{3}{2}}}{e^{x} + 1} dx. \tag{B5}$$

Here, $g_{\gamma'} = 3$ and $g_D = 4$. For total ζ , we need energy and pressure densities for both the visible and the hidden sectors, and we use the relation

$$\zeta = \frac{3}{4} \left(1 + \frac{p_v + p_h}{\rho_v + \rho_h} \right).$$
 (B6)

Before proceeding further, we note that the extension to include both the kinetic and mass mixings in Eqs. (3.2)–(B3) is straightforward as has been discussed in [9], and we exhibit them here for easy reference to guide the discussion in Sec. VII. With inclusion of both the kinetic mixing parameter δ and the mass mixing parameter $\epsilon = M_2/M_1$, the neutral current Lagrangian in the hidden sector takes the form

$$\mathcal{L}_{NC}^{\text{hid}} = \bar{D}\gamma^{\mu} [\epsilon_{\gamma'}^{D} A_{\mu}^{\gamma'} + \epsilon_{Z}^{D} Z_{\mu} + \epsilon_{\gamma}^{D} A_{\mu}^{\gamma}] D, \qquad (B7)$$

where

$$\epsilon_{\gamma'}^{D} \simeq g_{X}Q_{X}, \qquad \epsilon_{Z}^{D} \simeq \bar{\epsilon}g_{X}Q_{X}\sin\theta\left[1 + \frac{\delta}{\bar{\epsilon}}\right],$$

$$\epsilon_{\gamma}^{D} \simeq -\bar{\epsilon}g_{X}Q_{X}\cos\theta\left[1 + \frac{\delta}{\bar{\epsilon}}\right], \tag{B8}$$

where $\bar{\epsilon}$ is defined so that $\bar{\epsilon} = (\epsilon - \delta)/\sqrt{1 - \delta^2}$. There is also a corresponding modification of the neutral current in the visible sector as discussed in [9]. The constraints on δ and ϵ arising from the fits to the electroweak data are mild, and one finds that $|\epsilon - \delta|$ can be as large as 0.05, consistent with the same level of χ^2 fits to the electroweak data as the standard model [9].

APPENDIX C: SELF-INTERACTIONG DARK MATTER CROSS SECTIONS

1.
$$D\bar{D} \rightarrow D\bar{D}$$

Let us first consider $D\bar{D} \to D\bar{D}$ scattering. Here, the wave function for scattering of a plane wave scattering from

a central potential is given by $\psi(\vec{r}) \sim [e^{ikz} + f(\theta)e^{ikr}/r]$. In this case, the scattering amplitude $f(\theta)$ has an expansion in terms of the partial wave amplitudes $f_l = \frac{e^{i\delta_l}\sin\delta_l}{k}$, where δ_l is the phase shift for the lth partial wave so that $f(\theta)$ has the expansion $f(\theta) = \sum_{l=0}^{\infty} (2l+1) f_l P_l(\cos\theta)$ and σ_{tot}^{DD} have the expansion

$$\sigma_{\text{total}}^{D\bar{D}} = \int |f(\theta)|^2 d\Omega = (4\pi) \sum_{l} (2l+1)|f_l|^2.$$
 (C1)

The transfer cross section is defined by

$$\sigma_T^{D\bar{D}} = \int |f(\theta)|^2 (1 - \cos \theta) d\Omega. \tag{C2}$$

Using the relations

$$\int (dx)xP_{l}(x)P_{l'}(x) = \begin{cases} \frac{2(l'+1)}{(2l'+1)(2l'+3)} & \text{for } l = l'+1\\ \frac{2l'}{(2l'-1)(2l'+1)} & \text{for } l = l'-1, \end{cases}$$
(C3)

the transfer cross section can be written as

$$\sigma_T^{D\bar{D}} = 4\pi \sum_{l=0}^{\infty} ((2l+1)|f_l|^2 - lf_l f_{l-1}^* - (l+1)f_l f_{l+1}^*).$$
(C4)

The viscosity cross section defined by

$$\sigma_V^{D\bar{D}} = \int |f(\theta)|^2 (1 - \cos^2 \theta) d\Omega \tag{C5}$$

can be expanded in terms of partial waves using the relations

$$\int (dx)x^2P_l(x)P_{l'}(x) = \begin{cases} \frac{2(l'+1)(l'+2)}{(2l'+1)(2l'+3)(2l'+5)} & \text{for } l = l'+2 \\ \frac{2(2l^2+2l'-1)}{(2l'-1)(2l'+1)(2l'+3)} & \text{for } l = l' \\ \frac{2l'(l'-1)}{(2l'-1)(2l'+1)(2l'-3)} & \text{for } l = l'-2, \end{cases}$$
(C6)

which gives

$$\sigma_{V}^{D\bar{D}} = 4\pi \sum_{l=0}^{\infty} \left(\frac{2(l^{2}+l-1)(2l+1)}{(2l-1)(2l+3)} |f_{l}|^{2} - \frac{(l-1)l}{(2l-1)} f_{l} f_{l-2}^{*} - \frac{(l+2)(l+1)}{(2l+3)} f_{l} f_{l+2}^{*} \right). \tag{C7}$$

2.
$$DD \rightarrow DD$$
, $\bar{D}\bar{D} \rightarrow \bar{D}\bar{D}$

Here, the scattering involves identical particles, which are fermions, so the overall wave function for the particles

must be antisymmetric. This can happen in two ways: (i) spin antisymmetric and space symmetric or (ii) spin symmetric and space antisymmetric. Now the two spin particles can have a total spin 1 (triplet state) or total spin is zero (singlet state). For the triplet state, the space wave function must be antisymmetric in $\theta \to \pi - \theta$, and for the singlet state, the space wave function must be symmetric. Thus, we have for $\sigma^{DD}(\theta)$ the expression

$$\sigma^{DD}(\theta) = \frac{3}{4} |f'(\theta) - f'(\pi - \theta)|^2 + \frac{1}{4} |f'(\theta) + f'(\pi + \theta)|^2$$
$$= |f'(\theta)|^2 + |f'(\pi - \theta)|^2 - \text{Re}(f'(\theta)f'^*(\pi - \theta)). \tag{C8}$$

Further, σ_{tot}^{DD} is given by

$$\sigma_{\text{tot}}^{DD} = \frac{1}{2} \int \sigma^{DD}(\theta) d\Omega, \tag{C9}$$

where the front factor of 1/2 is to take account of the identical nature of the scattering particles. The partial wave analysis of σ_{tot}^{DD} gives

$$\sigma_{\text{tot}}^{DD} = 2\pi \sum_{l} (2l+1) \left[|f_{l}|^{2} + 2 \left[1 - \frac{1}{2} (-1)^{l} \right] |f'_{l}|^{2} \right]. \quad (C10)$$

Here, $f'_l = e^{i\delta'_l} \sin \delta'_l$ since the potential governing $DD \to DD$ scattering is different from the one that governs $D\bar{D} \to D\bar{D}$ scattering. Similar calculations are done for the transfer cross section and for viscosity cross section. Further, $\sigma^{\bar{D}\bar{D}}_{tof} = \sigma^{DD}_{tof}$.

APPENDIX D: ENTROPY CONSERVATION APPROXIMATION

Here, in Sec. D 1, we will discuss the validity of separate entropy conservation approximation for visible and hidden sectors, and in Sec. D 2, we will discuss the validity of the conservation of the total entropy which is the sum of the visible and the hidden sector entropies.

1. On the validity of separate entropy conservation approximation of visible and hidden sector

In several previous works (see, e.g., [29]), an assumption of entropy conservation per comoving volume separately for the visible and the hidden sectors is made to relate $\xi(T)$ at different temperatures. The above implies that the ratio s_h/s_v is unchanged at different temperatures, where s_v and s_h are the entropy densities for the visible and the hidden sectors, where

$$s_v = \frac{2\pi^2}{45} h_{\text{eff}}^v T^3, \qquad s_h = \frac{2\pi^2}{45} h_{\text{eff}}^h T_h^3.$$
 (D1)

Specifically it is assumed that the following relation between the temperatures T_0 and T holds:

$$\frac{h_{\text{eff}}^{h}(T_{h})}{h_{\text{eff}}^{v}(T)}\xi^{3}(T) = \frac{h_{\text{eff}}^{h}(T_{0h})}{h_{\text{eff}}^{v}(T_{0})}\xi^{3}(T_{0}). \tag{D2}$$

Noting that $T_h = \xi(T)T$ and $T_{0h} = \xi_0 T_0$, where $\xi_0 \equiv \xi(T_0)$, we can write the above equation as follows:

$$(h_{\rm eff}^h(\xi(T)T))^{1/3}\xi(T) = (h_{\rm eff}^v(T))^{1/3} \left(\frac{h_{\rm eff}^h(\xi_0T_0)}{h_{\rm eff}^v(T_0)}\right)^{1/3}\xi(T_0). \tag{D3}$$

Note that the left-hand side is a highly nonlinear function of $\xi(T)$ since for our model

$$h_{\text{eff}}^{\gamma'}(T_h) = \frac{45}{4\pi^4} \int_{x_{h\gamma'}}^{\infty} \frac{\sqrt{x^2 - x_{h\gamma'}^2}}{e^x - 1} (4x^2 - x_{h\gamma'}^2) dx,$$

$$h_{\text{eff}}^D(T_h) = \frac{15}{\pi^4} \int_{x_{hD}}^{\infty} \frac{\sqrt{x^2 - x_{hD}^2}}{e^x + 1} (4x^2 - x_{hD}^2) dx,$$
(D4)

where $x_{h\gamma'} = m_{\gamma'}/(T_h) = m_{\gamma'}/(\xi(T)T)$ and $x_{hD} = m_D/(\xi(T)T)$.

In Fig. 11, we give a comparison of the analysis of the evolution of the $\xi(T)$ using Eq. (2.15) vs the evolution given by the approximation of entropy conservation in comoving volume for the visible and the hidden sectors separately. The analysis shows that as ξ_0 gets progressively smaller, deviations of the approximate solutions gets progressively worse, and especially in the freeze-in region where $\xi_0 = 0.001$, the deviations of the approximate from the exact is huge for temperatures in the visible sector below 10^5 GeV. More importantly, for any choice of ξ_0 in

the range (0,1), which includes both the freeze-out and the freeze-in regions, the prediction of ξ_0 for the approximation is always inaccurate at the BBN temperature of ~1 MeV. The right panel gives a plot of ξ as a function of the visible sector temperature for different values of δ for the case when $\xi_0=0.001$. Here, one finds that the approximation (dashed line) gives a reasonably accurate result for the case when $\delta=0$; i.e., there is no kinetic mixing, but it gives highly inaccurate results for the case when δ in non-vanishing, even as small as $\delta \sim 10^{-10}$.

In the analysis done so far, we assumed $M_2 = 0$. For generality, we consider now the case where we include the mass mixing parameter ϵ along with kinetic mixing δ . Thus, we discuss again the thermal evolution when there are both kinetic mixing and mass mixing present where we use the relations given by Eqs. (B7) and (B8) and related relations given in [9]. In Fig. 12, we investigate the effect of including ϵ along δ on the evolution of $\xi(T)$. The left panel is for the case $\epsilon = 0.9\delta$ with $\delta = 4 \times 10^{-8}$, and as expected, the evolution for different ξ_0 shows a pattern similar to the left panel of Fig. 11. The right panel of Fig. 12 shows that evolutions with different ϵ follow a similar path at high temperatures but begin to separate at $T \sim 10$ GeV. This separation results in significantly different values of $\xi(T)$ at BBN temperature. As expected, we find that since δ and ϵ together control the thermal evolution, there is a significant difference in the pattern of evolution here relative to those of Fig. 11. However, for both Figs. 11 and 12, one finds that the predictions for $\xi(T)$ given by the approximation equation Eq. (D2) shown by dashed curves differ by wide margins from the result using Eq. (2.15) over wide regions of the parameter space and specifically at BBN temperature. Thus, our conclusion is that the entropy conservation approximation separately for the visible and hidden sectors in thermal evolution is not suitable for a precision analysis.

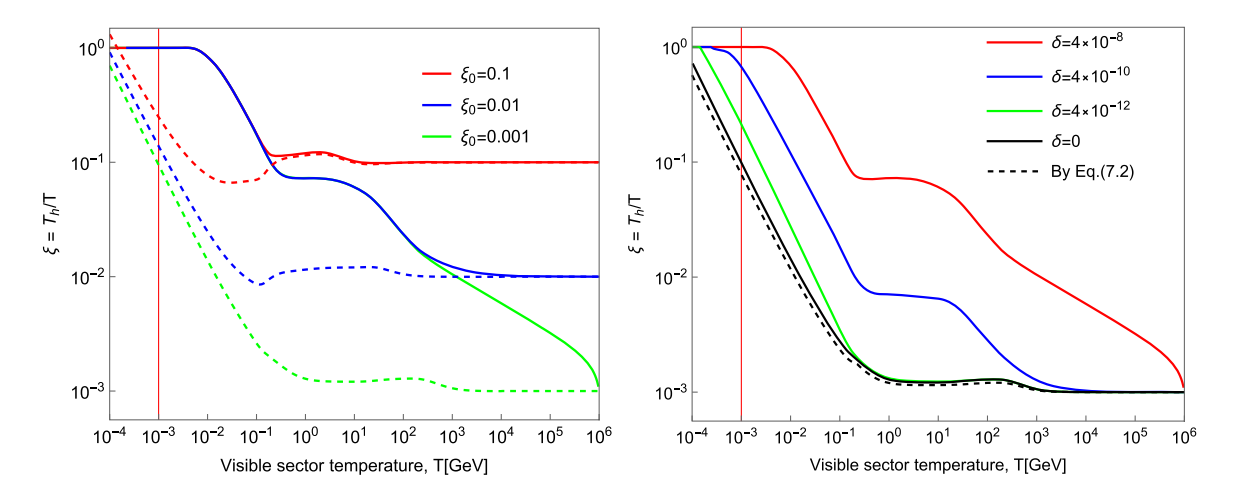


FIG. 11. Evolution of $\xi(T)$ with different initial condition using Eq. (2.15) of this paper (solid) and using the approximation of entropy conservation (dashed). Left panel: Here, $\delta=4\times10^{-8}$, and analysis is given for three widely different values of ξ_0 , i.e., $\xi_0=0.001$, $\xi_0=0.01$, $\xi_0=0.1$. Right panel: Here, $\xi_0=0.001$, and an analysis for several different values for δ in the range $\delta=0$ to $\delta=10^{-8}$ is exhibited. The rest of parameters are chosen so that $m_D=2$ GeV, $m_{\gamma'}=2$ MeV, $g_X=0.015$.

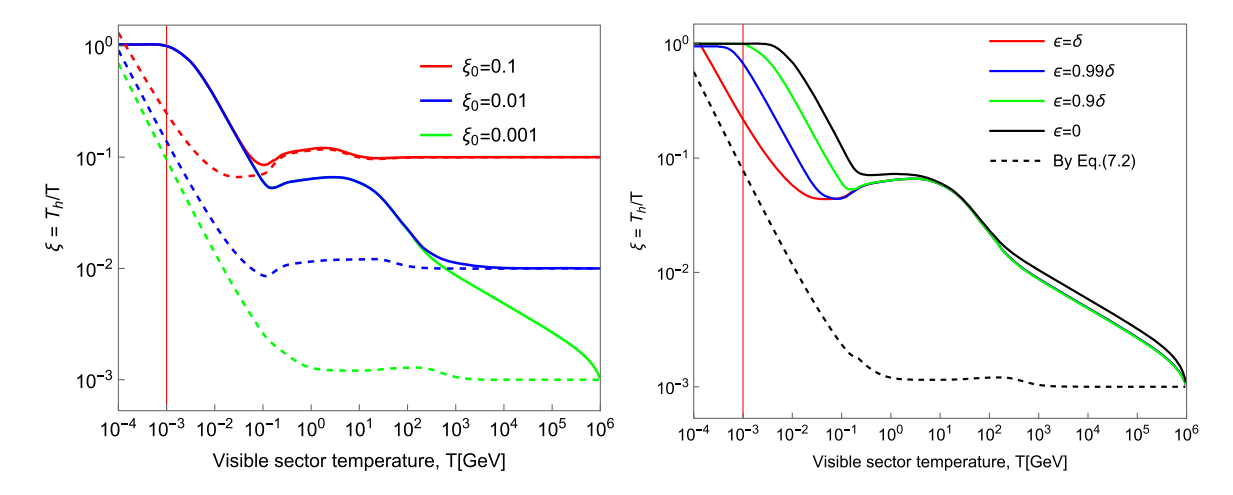


FIG. 12. Evolution of $\xi(T)$ with different initial conditions using Eq. (2.15) of this paper (solid) and using the approximation of entropy conservation (dashed). Left panel: Here, $\epsilon = 0.9\delta$, and the plot is for three different values of ξ_0 as shown. Right panel: Here, $\xi_0 = 0.001$, and the plots are for several different values of ϵ . For both the left and the right panels, the rest of parameters are chosen to be $m_D = 2$ GeV, $m_{\gamma'} = 2$ MeV, $g_X = 0.015$, $\delta = 4 \times 10^{-8}$.

2. On the validity of the total entropy conservation

In the preceding analysis, we discussed the evolution of $\xi(T)$ for the case when entropy conservation per comoving volume is assumed separately for the visible and the hidden sectors vs the case when the entropy conservation is assumed only for their sum. It is found that the deviations between the two analysis could be significant, as exhibited by Figs. 11 and 12. It is then pertinent to ask the validity of conservation of total entropy since the total entropy itself in not conserved either unless various sectors themselves equilibrate. We note that in our analysis the deduction of

the evolution equation for $\xi(T)$ did not involve any assumptions related to entropy, and the only place where the conservation of the total entropy was used was in the yield equations. For this reason, we reconsider the Botzmann equation for the yields without the assumption of total entropy conservation. We focus on the yield equation for the D fermion, which constitutes dark matter in the model and the analysis for the yield for the dark photon is very similar.

Thus, we start with the Boltzmann equation for the number density n_D , which is given by

$$\frac{dn_D}{dt} + 3Hn_D = C_D = \left[\langle \sigma v \rangle_{D\bar{D} \to i\bar{i}} (T) n_D^{\text{eq}} (T)^2 - \langle \sigma v \rangle_{D\bar{D} \to \gamma'\bar{\gamma}} (T_h) n_D (T_h)^2 + \langle \sigma v \rangle_{\gamma'\bar{\gamma} \to D\bar{D}} (T_h) n_{\gamma'} (T_h)^2 \right]. \tag{D5}$$

We note now that the equation for the yield $Y_D = n_D/\mathbf{s}$ without the use of entropy conservation gives so that

$$\begin{split} \frac{dY_D}{dT} &= \frac{1}{\mathbf{s}} \frac{dn_D}{dT} - \frac{n_s}{\mathbf{s}^2} \frac{d\mathbf{s}}{dT} \\ &= -\frac{\mathbf{s}}{H} \frac{d\rho_v/dT}{4\zeta\rho - 4\zeta_h\rho_h + j_h/H} \left(\frac{C_D}{\mathbf{s}^2}\right) + \frac{Y_D}{4H\mathbf{s}\zeta\rho} \left(\frac{d\rho}{dT}\right) \Delta_{\mathbf{s}}. \\ \Delta_{\mathbf{s}} &= \left[\frac{d\mathbf{s}}{dt} + 3H\mathbf{s}\right] \end{split} \tag{D6}$$

We notice that the set of terms on the right-hand side of Eq. (D6) involving C_D are exactly what we have in Eq. (4.1). Further, the term involving Δ_s vanishes on using the conservation of total entropy and indicates the deviation of the exact equation from the approximate one where total entropy conservation is assume. A similar analysis holds for the case of the dark photon yield equation. Thus, we carry out an analysis using the exact equations without

entropy conservation constraint and compare it with the analysis where entropy conservation is assumed. Results are presented in Fig. 13. The analysis of Fig. 13 shows that when the conservation of entropy (COE) is dropped, the results do not change a lot. Thus the top left panel for $\xi_0 = 0.01$ shows that the yield Y_D changes by typically within $\sim 15\%$ without inclusion of the entropy conservation constraint. A similar analysis holds for the case $\xi_0 = 1$, as shown on the right panel of Fig. 13. However, we point out an issue that arises at very low temperatures. Without COE constraint, the yields begin to exhibit an instability at low temperature at around 10^{-4} GeV. In part, this could be due to lack of analytic expressions for the entropy degrees of freedom in the visible sector where on relies on curves or tabulated data (see, e.g., [5,6]) because of hadronization of quarks and gluons. The instability arises essentially from the terms proportional to Δ_s . A proper analysis of this issue is outside the scope of this work and a relevant topic for further investigation.

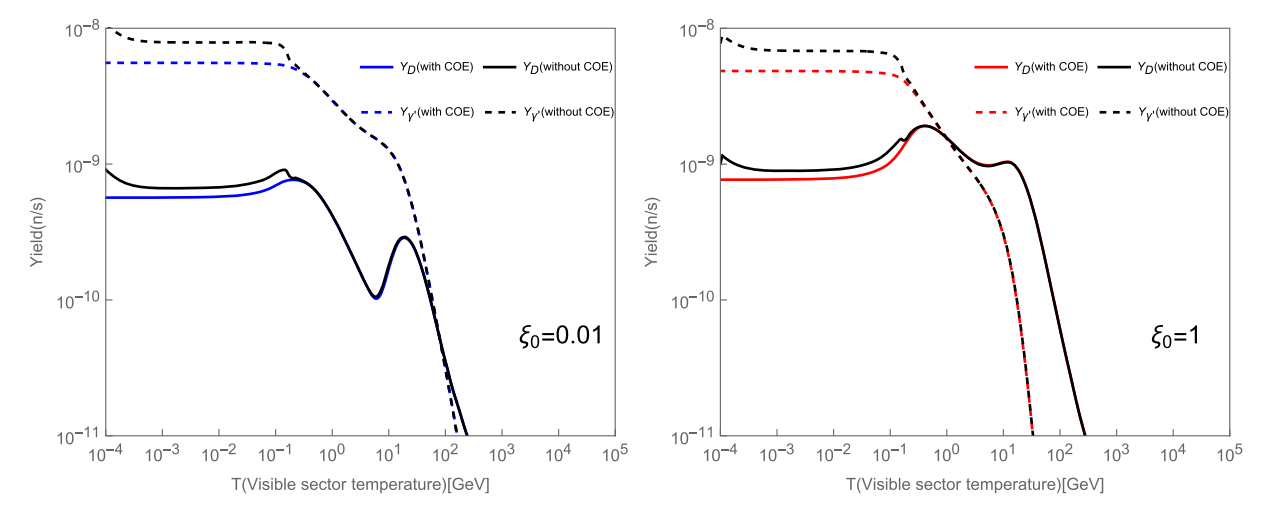


FIG. 13. Left panel: Yields of dark fermion and dark photon when $\xi_0 = 0.01$ with and without conversation of entropy (COE). Right panel: Evolution of $\xi(T)$ when $\xi_0 = 1$ with and without COE. The model point we used here is the same as Fig. 1, which is model (f) of Table I.

- [1] B. Holdom, Phys. Lett. 166B, 196 (1986).
- [2] B. Kors and P. Nath, Phys. Lett. B **586**, 366 (2004).
- [3] A. Aboubrahim and P. Nath, J. High Energy Phys. 09 (2022) 084.
- [4] G. Bélanger, F. Boudjema, A. Goudelis, A. Pukhov, and B. Zaldivar, Comput. Phys. Commun. 231, 173 (2018).
- [5] M. Hindmarsh and O. Philipsen, Phys. Rev. D 71, 087302 (2005).
- [6] L. Husdal, Galaxies 4, 78 (2016).
- [7] B. Patt and F. Wilczek, arXiv:hep-ph/0605188.
- [8] B. Kors and P. Nath, J. High Energy Phys. 07 (2005) 069.
- [9] D. Feldman, Z. Liu, and P. Nath, Phys. Rev. D 75, 115001 (2007).
- [10] M. Du, Z. Liu, and P. Nath, Phys. Lett. B **834**, 137454 (2022).
- [11] A. Aboubrahim, W. Z. Feng, P. Nath, and Z. Y. Wang, Phys. Rev. D 103, 075014 (2021).
- [12] A. Aboubrahim and P. Nath, Phys. Rev. D 99, 055037 (2019).
- [13] A. Aboubrahim, P. Nath, and Z. Y. Wang, J. High Energy Phys. 12 (2021) 148.
- [14] X. Chen and S. H. H. Tye, J. Cosmol. Astropart. Phys. 06 (2006) 011.
- [15] D. Feldman, B. Kors, and P. Nath, Phys. Rev. D **75**, 023503 (2007).
- [16] D. Feldman, Z. Liu, and P. Nath, AIP Conf. Proc. 939, 50 (2007).
- [17] K. Cheung and T. C. Yuan, J. High Energy Phys. 03 (2007) 120.
- [18] W. Z. Feng, P. Nath, and G. Peim, Phys. Rev. D 85, 115016 (2012).
- [19] D. Feldman, P. Fileviez Perez, and P. Nath, J. High Energy Phys. 01 (2012) 038.

- [20] W. Z. Feng, A. Mazumdar, and P. Nath, Phys. Rev. D **88**, 036014 (2013).
- [21] X. Chen, J. Cosmol. Astropart. Phys. 09 (2009) 029.
- [22] M. R. Buckley and P. J. Fox, Phys. Rev. D **81**, 083522 (2010).
- [23] M. Ibe and H. b. Yu, Phys. Lett. B 692, 70 (2010).
- [24] J. L. Feng, M. Kaplinghat, H. Tu, and H. B. Yu, J. Cosmol. Astropart. Phys. 07 (2009) 004.
- [25] A. Loeb and N. Weiner, Phys. Rev. Lett. 106, 171302 (2011).
- [26] S. Tulin, H. B. Yu, and K. M. Zurek, Phys. Rev. Lett. 110, 111301 (2013).
- [27] S. Tulin, H.B. Yu, and K.M. Zurek, Phys. Rev. D 87, 115007 (2013).
- [28] K. Schutz and T. R. Slatyer, J. Cosmol. Astropart. Phys. 01 (2015) 021.
- [29] J. L. Feng, H. Tu, and H. B. Yu, J. Cosmol. Astropart. Phys. 10 (2008) 043.
- [30] J. Redondo and M. Postma, J. Cosmol. Astropart. Phys. 02 (2009) 005.
- [31] X. Chu, T. Hambye, and M. H. G. Tytgat, J. Cosmol. Astropart. Phys. 05 (2012) 034.
- [32] X. Chu, Y. Mambrini, J. Quevillon, and B. Zaldivar, J. Cosmol. Astropart. Phys. 01 (2014) 034.
- [33] M. Kaplinghat, S. Tulin, and H. B. Yu, Phys. Rev. Lett. 116, 041302 (2016).
- [34] R. T. D'Agnolo and J. T. Ruderman, Phys. Rev. Lett. 115, 061301 (2015).
- [35] E. Kuflik, M. Perelstein, N. R. L. Lorier, and Y. D. Tsai, Phys. Rev. Lett. 116, 221302 (2016).
- [36] T. Bringmann, F. Kahlhoefer, K. Schmidt-Hoberg, and P. Walia, Phys. Rev. Lett. **118**, 141802 (2017).
- [37] J. A. Evans, C. Gaidau, and J. Shelton, J. High Energy Phys. 01 (2020) 032.

- [38] L. Sagunski, S. Gad-Nasr, B. Colquhoun, A. Robertson, and S. Tulin, J. Cosmol. Astropart. Phys. 01 (2021) 024.
- [39] N. Fernandez, Y. Kahn, and J. Shelton, J. High Energy Phys. 07 (2022) 044.
- [40] K. Kaneta, H. S. Lee, and S. Yun, Phys. Rev. Lett. 118, 101802 (2017).
- [41] K. Kaneta, H. S. Lee, and S. Yun, Phys. Rev. D 95, 115032 (2017).
- [42] R. T. Co, A. Pierce, Z. Zhang, and Y. Zhao, Phys. Rev. D 99, 075002 (2019).
- [43] J. A. Dror, K. Harigaya, and V. Narayan, Phys. Rev. D 99, 035036 (2019).
- [44] P. Agrawal, N. Kitajima, M. Reece, T. Sekiguchi, and F. Takahashi, Phys. Lett. B **801**, 135136 (2020).
- [45] A. J. Long and L. T. Wang, Phys. Rev. D 99, 063529 (2019).
- [46] G. Alonso-Álvarez, T. Hugle, and J. Jaeckel, J. Cosmol. Astropart. Phys. 02 (2020) 014.
- [47] Y. Nakai, R. Namba, and Z. Wang, J. High Energy Phys. 12 (2020) 170.
- [48] G. Choi, T. T. Yanagida, and N. Yokozaki, J. High Energy Phys. 01 (2021) 057.
- [49] C. Delaunay, T. Ma, and Y. Soreq, J. High Energy Phys. 02 (2021) 010.
- [50] P. W. Graham, J. Mardon, and S. Rajendran, Phys. Rev. D 93, 103520 (2016).
- [51] Y. Ema, K. Nakayama, and Y. Tang, J. High Energy Phys. 07 (2019) 060.
- [52] A. Ahmed, B. Grzadkowski, and A. Socha, J. High Energy Phys. 08 (2020) 059.
- [53] J. Berger, K. Jedamzik, and D. G. E. Walker, J. Cosmol. Astropart. Phys. 11 (2016) 032.
- [54] M. Ibe, S. Kobayashi, Y. Nakayama, and S. Shirai, J. High Energy Phys. 04 (2020) 009.
- [55] S. D. McDermott and S. J. Witte, Phys. Rev. D 101, 063030 (2020).
- [56] A. Fradette, M. Pospelov, J. Pradler, and A. Ritz, Phys. Procedia **61**, 689 (2015).
- [57] I. M. Bloch, R. Essig, K. Tobioka, T. Volansky, and T. T. Yu, J. High Energy Phys. 06 (2017) 087.
- [58] M. Pospelov, A. Ritz, and M. B. Voloshin, Phys. Rev. D 78, 115012 (2008).
- [59] J. E. Kim and D. J. E. Marsh, Phys. Rev. D **93**, 025027 (2016).
- [60] L. Hui, J. P. Ostriker, S. Tremaine, and E. Witten, Phys. Rev. D 95, 043541 (2017).
- [61] J. Halverson, C. Long, and P. Nath, Phys. Rev. D 96, 056025 (2017).
- [62] C. Boehm, D. Hooper, J. Silk, M. Casse, and J. Paul, Phys. Rev. Lett. 92, 101301 (2004).
- [63] C. Boehm and P. Fayet, Nucl. Phys. B683, 219 (2004).
- [64] D. Feldman, Z. Liu, and P. Nath, Phys. Rev. D 79, 063509 (2009).
- [65] N. Arkani-Hamed, D. P. Finkbeiner, T. R. Slatyer, and N. Weiner, Phys. Rev. D 79, 015014 (2009).
- [66] M. Pospelov, A. Ritz, and M. B. Voloshin, Phys. Lett. B 662, 53 (2008).
- [67] L. Bergstrom, T. Bringmann, I. Cholis, D. Hooper, and C. Weniger, Phys. Rev. Lett. 111, 171101 (2013).

- [68] L. Bergstrom, T. Bringmann, and J. Edsjo, Phys. Rev. D 78, 103520 (2008).
- [69] A. Aboubrahim, W. Z. Feng, P. Nath, and Z. Y. Wang, J. High Energy Phys. 06 (2021) 086.
- [70] A. Aboubrahim, M. M. Altakach, M. Klasen, P. Nath, and Z. Y. Wang, J. High Energy Phys. 03 (2023) 182.
- [71] J. P. Lees *et al.* (*BABAR* Collaboration), Phys. Rev. Lett. **113**, 201801 (2014).
- [72] J. P. Lees *et al.* (*BABAR* Collaboration), Phys. Rev. Lett. **119**, 131804 (2017).
- [73] N. Baltzell *et al.* (HPS Collaboration), Nucl. Instrum. Methods Phys. Res., Sect. A **859**, 69 (2017).
- [74] R. Aaij *et al.* (LHCb Collaboration), Phys. Rev. Lett. **124**, 041801 (2020).
- [75] E. Kou *et al.* (Belle-II Collaboration), Prog. Theor. Exp. Phys. **2019**, 123C01 (2019); **2020**, 029201(E) (2020).
- [76] C. Ahdida *et al.* (SHiP Collaboration), Eur. Phys. J. C 81, 451 (2021).
- [77] A. Berlin, S. Gori, P. Schuster, and N. Toro, Phys. Rev. D 98, 035011 (2018).
- [78] Y. D. Tsai, P. deNiverville, and M. X. Liu, Phys. Rev. Lett. 126, 181801 (2021).
- [79] J. Blumlein and J. Brunner, Phys. Lett. B 701, 155 (2011).
- [80] J. Blümlein and J. Brunner, Phys. Lett. B 731, 320 (2014).
- [81] S. Andreas, C. Niebuhr, and A. Ringwald, Phys. Rev. D 86, 095019 (2012).
- [82] E. M. Riordan, M. W. Krasny, K. Lang, P. De Barbaro, A. Bodek, S. Dasu, N. Varelas, X. Wang, R. G. Arnold, D. Benton *et al.*, Phys. Rev. Lett. **59**, 755 (1987).
- [83] D. Banerjee et al. (NA64 Collaboration), Phys. Rev. D 101, 071101 (2020).
- [84] J. R. Batley *et al.* (NA48/2 Collaboration), Phys. Lett. B **746**, 178 (2015).
- [85] J. H. Chang, R. Essig, and S. D. McDermott, J. High Energy Phys. 01 (2017) 107.
- [86] H. An, M. Pospelov, and J. Pradler, Phys. Lett. B 725, 190 (2013).
- [87] R. Essig, E. Kuflik, S. D. McDermott, T. Volansky, and K. M. Zurek, J. High Energy Phys. 11 (2013) 193.
- [88] S. D. McDermott, H. H. Patel, and H. Ramani, Phys. Rev. D 97, 073005 (2018).
- [89] N. Aghanim *et al.* (Planck), Astron. Astrophys. **641**, A6 (2020); **652**, C4(E) (2021).
- [90] T. Hasegawa, N. Hiroshima, K. Kohri, R. S. L. Hansen, T. Tram, and S. Hannestad, J. Cosmol. Astropart. Phys. 12 (2019) 012.
- [91] M. Kawasaki, K. Kohri, and N. Sugiyama, Phys. Rev. Lett. 82, 4168 (1999).
- [92] A. H. Abdelhameed *et al.* (CRESST Collaboration), Phys. Rev. D **100**, 102002 (2019).
- [93] E. Aprile *et al.* (XENON Collaboration), Phys. Rev. Lett. **123**, 241803 (2019).
- [94] R. Iengo, J. High Energy Phys. 05 (2009) 024.
- [95] M. Lattanzi and J. I. Silk, Phys. Rev. D 79, 083523 (2009).
- [96] N. Arkani-Hamed, D. P. Finkbeiner, T. R. Slatyer, and N. Weiner, Phys. Rev. D 79, 015014 (2009).

- [97] S. Cassel, J. Phys. G 37, 105009 (2010).
- [98] M. Cirelli, A. Strumia, and M. Tamburini, Nucl. Phys. B787, 152 (2007).
- [99] L. Hulthen, Ark. Mat. Astron. Fys. 28A, 5 (1942).
- [100] Handbuch der Physik, edited by L. Hulthen, M. Sugawara, and S. Flugge (Springer, New York, 1957).
- [101] T. R. Slatyer, J. Cosmol. Astropart. Phys. 02 (2010) 028.
- [102] C. Kao, Y. L. Sming Tsai, and G. G. Wong, Phys. Rev. D 103, 055021 (2021).
- [103] S. Tulin and H. B. Yu, Phys. Rep. **730**, 1 (2018).
- [104] A. Robertson, D. Harvey, R. Massey, V. Eke, I.G. McCarthy, M. Jauzac, B. Li, and J. Schaye, Mon. Not. R. Astron. Soc. 488, 3646 (2019).
- [105] O. D. Elbert, J. S. Bullock, M. Kaplinghat, S. Garrison-Kimmel, A. S. Graus, and M. Rocha, Astrophys. J. 853, 109 (2018).
- [106] K. E. Andrade, J. Fuson, S. Gad-Nasr, D. Kong, Q. Minor, M. G. Roberts, and M. Kaplinghat, Mon. Not. R. Astron. Soc. 510, 54 (2021).
- [107] D. N. Spergel and P. J. Steinhardt, Phys. Rev. Lett. 84, 3760 (2000).
- [108] M. Vogelsberger, J. Zavala, and A. Loeb, Mon. Not. R. Astron. Soc. 423, 3740 (2012).
- [109] M. Rocha, A. H. G. Peter, J. S. Bullock, M. Kaplinghat, S. Garrison-Kimmel, J. Onorbe, and L. A. Moustakas, Mon. Not. R. Astron. Soc. 430, 81 (2013).
- [110] A. H. G. Peter, M. Rocha, J. S. Bullock, and M. Kaplinghat, Mon. Not. R. Astron. Soc. 430, 105 (2013).
- [111] J. Zavala, M. Vogelsberger, and M. G. Walker, Mon. Not. R. Astron. Soc. 431, L20 (2013).

- [112] O. D. Elbert, J. S. Bullock, S. Garrison-Kimmel, M. Rocha, J. Oñorbe, and A. H. G. Peter, Mon. Not. R. Astron. Soc. 453, 29 (2015).
- [113] M. Vogelsberger, J. Zavala, C. Simpson, and A. Jenkins, Mon. Not. R. Astron. Soc. 444, 3684 (2014).
- [114] A. B. Fry, F. Governato, A. Pontzen, T. Quinn, M. Tremmel, L. Anderson, H. Menon, A. M. Brooks, and J. Wadsley, Mon. Not. R. Astron. Soc. 452, 1468 (2015).
- [115] G. A. Dooley, A. H. G. Peter, M. Vogelsberger, J. Zavala, and A. Frebel, Mon. Not. R. Astron. Soc. 461, 710 (2016).
- [116] S. Girmohanta and R. Shrock, Phys. Rev. D **106**, 063013 (2022).
- [117] S. Girmohanta and R. Shrock, Phys. Rev. D 107, 063006 (2023).
- [118] R. N. Mohapatra, S. Nussinov, and V. L. Teplitz, Phys. Rev. D 66, 063002 (2002).
- [119] M. Vogelsberger, J. Zavala, F. Y. Cyr-Racine, C. Pfrommer, T. Bringmann, and K. Sigurdson, Mon. Not. R. Astron. Soc. 460, 1399 (2016).
- [120] J. M. Cline, Z. Liu, G. Moore, and W. Xue, Phys. Rev. D 89, 043514 (2014).
- [121] K. K. Boddy, M. Kaplinghat, A. Kwa, and A. H. G. Peter, Phys. Rev. D 94, 123017 (2016).
- [122] I. Rothstein and W. Skiba, Phys. Rev. D 65, 065002 (2002).
- [123] M. R. Douglas and G. W. Moore, arXiv:hep-th/9603167.
- [124] N. Arkani-Hamed, A. G. Cohen, and H. Georgi, Phys. Rev. Lett. 86, 4757 (2001).
- [125] C. T. Hill, S. Pokorski, and J. Wang, Phys. Rev. D 64, 105005 (2001).